



1 **Crossing hydrological and geochemical modeling to understand the spatiotemporal variability**

2 **of water chemistry in an elementary watershed (Strengbach, France)**

3 Julien Ackerer, Benjamin Jeannot, Frederick Delay, Sylvain Weill, Yann Lucas, Bertrand Fritz,

4 Daniel Viville, François Chabaux

5 Laboratoire d'Hydrologie et de Géochimie de Strasbourg, Université de Strasbourg, CNRS,

6 ENGEES, 1 rue Blessig, 67084 Strasbourg Cedex, France

7

8

9

10

11

12

13

14

15

16

17

18



19 **Abstract**

20 Understanding the spatiotemporal variability of the chemical composition of surface waters is a
21 major issue for the scientific community, especially given the prospect of significant
22 environmental changes for the next decades. To date, the study of concentration-discharge
23 relationships has been intensively used to assess the spatiotemporal variability of the water
24 chemistry at watershed scales. However, the lack of independent estimations of the water
25 transit times within catchments limits our ability to model and predict the water chemistry with
26 only geochemical approaches. This study demonstrates the potential of coupling hydrological
27 and hydrogeochemical modeling to better understand the spatiotemporal variability of the
28 composition of surface waters. In a first step, a dimensionally reduced hydrological model
29 coupling surface flow with subsurface flow (i.e., the Normally Integrated Hydrological Model,
30 NIHM) has been used to constrain the distribution of the flow lines that are feeding the springs.
31 In a second step, hydrogeochemical simulations with the code KIRMAT (Kinetic Reaction and
32 MAss Transport) have been performed to calculate the evolution of the water chemistry along
33 the flow lines. The results indicate that the concentrations of dissolved silica (H_4SiO_4) and in
34 basic cations (Na^+ , K^+ , Mg^{2+} , and Ca^{2+}) in the spring waters are correctly reproduced with a
35 simple integration along the flow lines. The results also show that the modest variabilities of the
36 flow line distribution and of the flow velocity imply that the water transit times only vary from
37 approximately 1.5 to 3 months from floods to drought events. These findings demonstrate that
38 the chemostatic behavior of the spring chemistry is a direct consequence of the strong
39 hydrological control of the water transit times within the catchment. The good matching
40 between the measured and modeled concentrations while respecting the water-rock interaction



41 times provided by the hydrological simulations also shows that it is possible to capture the
42 chemical composition of waters using simply determined reactive surfaces and experimental
43 kinetic constants. The results of our simulation strengthen the idea that the low surfaces
44 calculated from the geometrical shapes of minerals are a good estimate of the reactive surfaces
45 within the natural environment and certainly the one to be used for hydrogeochemical
46 modeling such as that performed in this work. Overall, this work shows that the
47 hydrogeochemical functioning of an elementary watershed, such as the Strengbach catchment,
48 is relatively simple. The acquisition and variability of the water chemistry can be explained
49 through process-based modeling approaches and by only formulating few hypotheses on the
50 functioning of the watershed.

51



52 **1- Introduction**

53 Understanding the effects of the ongoing climatic changes on the environment is a major issue
54 for the coming years. The global increase of temperature is expected to affect the hydrological
55 cycle at a large scale and providing a precise estimation of its repercussion on the evolution of
56 soils and on the chemistry of waters remains challenging. That results from the wide diversity of
57 hydrological, geochemical, and biological processes, and of their coupling, that operate at the
58 Earth's surface (e.g., Gislason et al., 2009; Goddérís et al., 2013; Beaulieu et al., 2012; 2016).
59 Forecasting the evolution of the Earth's surface relies on our ability to develop process-based
60 models integrating a large number of processes over different spatial and temporal scales. This
61 is especially the case for modeling the variability of the water geochemical composition at a
62 watershed scale, which requires the development of modeling codes able to combine, as closely
63 as possible, hydrological and geochemical processes (Kirchner, 2006).

64 Recent efforts in hydrological modeling were conducted to develop spatially distributed
65 approaches that better consider the interplay between surface and subsurface processes (e.g.,
66 Gunduz and Aral, 2005; Kampf and Burges, 2007; Camporese et al., 2010). Due to the
67 complexity of flows in the hydrological processes, many modeling approaches are based on the
68 full resolution of Richard's and Saint Venant equations to correctly describe the interactions
69 between stream, overland and subsurface waters (Kampf and Burges, 2007). These approaches
70 have shown their ability to capture the hydrological functioning of various watersheds, knowing
71 that the full resolution of Richard's and Saint Venant equations requires long computational
72 times and faces calibration and parameterization difficulties (Ebel and Loague, 2006; Mirus et
73 al., 2011). Questions have been raised regarding the optimal complexity of the equations that



74 are needed to correctly treat the hydrology of catchments in their surface and subsurface
75 compartments with reasonable computation times (Gunduz and Aral, 2005). Low-dimensional
76 and depth-integrated models have attracted growing interest because they represent an
77 interesting compromise between equation complexity, computational time, and result accuracy
78 (Pan et al., 2015; Hazenberg et al., 2016; Weill et al., 2013; 2017; Jeannot et al., 2018). These
79 depth-integrated models recently demonstrated their ability to reproduce the results from fully
80 dimensioned approaches in small catchments while reducing computational costs (Pan et al.,
81 2015; Jeannot et al., 2018). Nonetheless, the water transit times calculated from these depth-
82 integrated models are rarely confronted with the water-rock interaction times inferred from
83 hydrogeochemical modeling of water chemistry in watersheds.

84 For its part, the understanding of the hydrogeochemical functioning of the critical zone has
85 been significantly advanced by the implementation of reactive-transport laws in geochemical
86 modeling codes (Steeffel et al., 2005; Lucas et al., 2010; 2017; Godd ris et al., 2013; Li et al.,
87 2017). These developments allow for considering a variety of processes, such as flow and
88 transport processes, ion exchanges, biogeochemical reactions, and the interplay between
89 primary mineral dissolution and secondary mineral precipitation (Moore et al., 2012; Lebedeva
90 and Brantley, 2013; Ackerer et al., 2018). Reactive transport models have been used to explore
91 a wide variety of scientific issues, including the study of global atmospheric CO₂ consumption by
92 weathering reactions (Godd ris et al., 2013; Li et al., 2014), the formation and evolution of soil
93 and regolith profiles (Maher et al., 2009; Navarre-Sitchler et al., 2009; Lebedeva and Brantley,
94 2013), and the variability of water chemistry in the environment (Lucas et al., 2010; 2017;
95 Ackerer et al., 2018). However, these approaches usually rely on a simple 1D flow path through



96 a regolith column or along a hill slope to model flow in the system (e.g., Maher et al., 2011;
97 Moore et al., 2012; Lucas et al., 2017; Ackerer et al., 2018). If these approaches are useful to
98 discuss the key processes involved in regolith formation and in the acquisition of the water
99 chemical composition, such 1D transport reactive modeling cannot take into account the
100 diversity or the complexity of the flow trajectories in watersheds; hence, its effects on the water
101 chemistry at the watershed scale.

102 A new step is therefore necessary for the development of hydrogeochemical modeling
103 approaches that are applicable at the watershed scale and are able to integrate the complexity
104 of the water flows and the diversity of the water-rock interaction processes. This is the aim of
105 this work, which combines for the first time in this manner the results from a hydrological
106 depth-integrated and spatially distributed model (NIHM) with a reactive-transport model
107 (KIRMAT). This coupling allows for modeling the spatial and temporal simulation of the flow
108 trajectories, the flow rates, the weathering reactions, and the evolution of the water chemistry
109 within an elementary watershed, the Strengbach catchment. This catchment is one of the
110 reference observatories of the French critical zone network (OZCAR), where multidisciplinary
111 studies, including hydrological, geochemical and geological investigations, have been performed
112 since 1986 (“Observatoire Hydrogéochimique de l’Environnement”, OHGE;
113 <http://ohge.unistra.fr>; El Gh’Mari, 1995; Fichter et al., 1998; Viville et al., 2012; Gangloff et al.,
114 2014; 2016; Pierret et al., 2014; Prunier et al., 2015; Pan et al., 2015; Ackerer et al., 2016; 2018;
115 Beaulieu et al., 2016; Chabaux et al., 2017; Schmitt et al., 2017; 2018; Daval et al., 2018). The
116 method proposed in this work will yield precise knowledge of the water flow paths and their
117 variability from wet to dry seasons, which is an important new step to better constrain the



118 water transit times within catchments and to correctly understand the seasonal fluctuations in
119 water chemistry.

120 **2- Site presentation and data acquisition**

121 The Strengbach catchment is a small watershed (0.8 km²) located in the Vosges Mountains of
122 northeastern France at altitudes between 883 and 1147 omsl. Its hydroclimatic characteristics
123 can be found in Viville et al. (2012) or in Pierret et al. (2014). It is marked by a mountainous
124 oceanic climate, with an annual mean temperature of 6 °C and an annual mean rainfall of
125 approximately 1400 mm, with 15 to 20% falling as snow during two to four months per year.
126 The snow cover period is quite variable from year to year, and may not be continuous over the
127 entire winter. The annual mean evapotranspiration is of approximately 600 mm, and the annual
128 mean runoff of approximately 800 mm (in Viville et al., 2012). The watershed is currently
129 covered by a beech and spruce forest. The bedrock is a base-poor Hercynian granite covered by
130 a 50 to 100 cm-thick acidic and coarse-in-texture soil. The granitic bedrock was fractured and
131 hydrothermally altered, with a stronger degree of hydrothermal overprinting in the northern
132 than the southern part of the catchment (Fichter et al., 1998). The granite was also affected by
133 surface weathering processes during the Quaternary (Ackerer et al., 2016). The porous and
134 uppermost part of the granitic basement constitutes an aquifer from 2 to approximately 10
135 meters thickness. In the Strengbach watershed, the major floods and high-flow events usually
136 occur during snowmelt periods at the end of the winter season or in the early spring. In
137 contrast, the low-flow periods commonly happen at the end of the summer or during the
138 autumn. Several springs naturally emerge along the slopes (figure 1). The watershed has also
139 been equipped with several piezometers and boreholes since 2012, those being located along



140 the slopes on both sides of the watershed (figure 1; Chabaux et al., 2017). Spring waters are
141 regularly collected and analyzed since 2005, with a sampling frequency allowing for covering the
142 entire range of water discharges from important droughts to strong flood events. Piezometer
143 waters have been collected during sampling campaigns since 2012, and as for the spring waters,
144 these sampling campaigns cover all the types of hydrological conditions encountered at the
145 Strengbach catchment. The soil solutions are also regularly collected on the southern slope at a
146 beech site (named HP) and to the north at a spruce site (named VP; figure 1; more details are
147 provided in Prunier et al., 2015). For all the collected waters, the concentrations of the major
148 dissolved species and the pH were determined by following the analytical techniques used at
149 LHyGeS (Strasbourg, France) and detailed in Gangloff et al. (2014) and Prunier et al. (2015).
150 Discharges of water from the springs were measured during the sampling campaigns, as were
151 the water levels within the piezometers. The mineralogy and the porosity of the bedrock have
152 been studied in detail in previous studies (El Gh'Mari, 1995; Fichter et al., 1998). On the
153 southern part of the catchment, the weakly hydrothermally altered granite (named HPT, figure
154 1) is mainly composed of quartz (35%), albite (31%), K-feldspar (22%) and biotite (6%). It also
155 contains small amounts of muscovite (3%), anorthite (2%), apatite (0.5%) and clay minerals
156 (0.5%). On the northern part of the catchment, the lithology is more variable, with the presence
157 of gneiss close to the crest lines and the occurrence of hydrothermally altered granite on the
158 rest of the slopes (El Gh'Mari, 1995, figure 1). The hydrological, geochemical and petrological
159 data obtained from these field investigations are the basis of the modeling work presented in
160 the following. More precisely, this study is based on hydrogeochemical data from 2005 to 2015
161 for waters from four springs of the southern part (CS1, CS2, CS3 and CS4) and one spring of the



162 northern part (RH3) of the watershed. Hydrogeochemical data obtained over the period 2012-
163 2015 for two piezometers (PZ3, PZ5) of the southern part of the watershed are also studied. The
164 chemical data from spring and piezometer waters modeled this study are reported in Table 1.

165 **3- Modeling methods**

166 The modeling developments presented in this study constitute a new step in the efforts
167 undertaken at LHyGeS to constrain the mechanisms controlling the acquisition of geochemical
168 composition of surface waters and to understand their spatial and temporal variations at the
169 scale of elementary mountainous watersheds (Schaffhauser et al., 2014; Lucas et al., 2017;
170 Ackerer et al., 2018). The main innovation of this work is to couple a spatially distributed
171 hydrological model with a reactive transport model to constrain the spatiotemporal variability
172 of chemical composition of spring and piezometer waters from the Strengbach watershed. To
173 the best of our knowledge, this is the first time that such a coupling between hydrological and
174 hydrogeochemical modeling approaches has been attempted at the watershed scale. In the
175 present study, the hydrological model determines the distribution of the water flow lines within
176 the watershed and thus constrains the water transit times for any period (summer or fall
177 droughts, winter or spring floods). Then, the hydrogeochemical model is used to simulate the
178 acquisition and the evolution of the water chemistry along the determined flow lines within the
179 catchment.

180 **3-1 Hydrological modeling**

181 To assess the water flows in the watershed, several simulations were performed with the
182 hydrological code NIHM (Normally Integrated Hydrological Model; Pan et al., 2015; Weill et al.,



183 2017; Jeannot et al., 2018). This code is a coupled stream, overland, and depth-integrated
184 subsurface flow model developed at LHyGeS and already tested in the Strengbach watershed
185 (Pan et al., 2015). The stream and overland flows are described by a diffusive-wave equation,
186 and the subsurface flow is handled through an integration (in a direction normal to bedrock) of
187 the unsaturated-saturated flow equation from the bedrock to the soil surface (Weill et al.,
188 2017). The water exchanges between the surface and subsurface flows are addressed via the
189 hydraulic head differences between the two compartments (Jeannot et al., 2018). First,
190 numerical simulations were performed to correctly reproduce the water discharges from the
191 Strengbach stream at the outlet of the watershed between 2010 and 2015 (figure 2). The
192 thickness of the aquifer that was used for the simulations varied from 2 meters near the main
193 crests to up to 8 meters in the middle of the watershed (figure 2), in agreement with the data
194 obtained during the recent geological investigations and drilling campaigns undertaken at the
195 catchment (Ackerer et al., 2016; Chabaux et al., 2017). The uniform precipitations over space
196 applied at the surface of the catchment are drawn from data of the pluviometric station located
197 at the highest elevation of the watershed (site PA, figure 1). Once the water discharges were
198 correctly reproduced at the outlet, a backtracking approach was used to constrain the origin of
199 subsurface water exiting the system at prescribed locations, and the spatiotemporal variability
200 of the flow lines within the watershed. To back track the water particles, the velocity fields
201 calculated by the NIHM model were inverted in their direction, and the locations of the
202 backtracked particles were saved at each time-step. A daily time-step was used for the
203 backtracking, as a compromise between computational efforts and a refined description of the
204 transient velocity fields. A schematic representation of the backtracking approach is given in



205 figure 3. This methodology allows for constraining the flow lines that bring the waters for a
206 given time and at a given position on the catchment. This information is of major interest to
207 determine the origin of the spring and piezometer waters. It is shown at the catchment scale,
208 that flows are mainly driven by gravity in association with the steep slopes of the watershed,
209 the latter being almost evenly drained over its whole surface area (figure 4). For each water
210 sampling area, ten flow lines that bring water to the location of interest were determined
211 (figure 4), together with a few features of the flow lines, including: local velocities, mean
212 velocities, and length of the flow paths. It is worth noting that streamlines calculated via
213 backtracking only consider flow in the subsurface compartment and are conditional to an arrival
214 date at a prescribed location. Therefore, times calculated along the streamlines correspond to a
215 date, x days before arrival, at which a water particle entered the subsurface or passed at a given
216 location along the streamline. As streamlines are not associated with mean water flux values,
217 the time distributions drawn from streamline calculations are only an approximation of the
218 actual transit time distributions.

219 **3-2 Hydrogeochemical modeling**

220 The simulations of the water chemical composition along the flow lines were performed with
221 the hydrogeochemical KIRMAT code (Kinetic of Reaction and MAss Transport; Gérard et al.,
222 1998; Lucas et al., 2010; Ngo et al., 2014). KIRMAT is a thermokinetic model that simultaneously
223 solves equations describing geochemical reactions and transport mass balances in a 1D-porous
224 medium. The mass transport includes the effects of one-dimensional convection, diffusion and
225 kinematic dispersion. Chemical reactions account for the dissolution of primary minerals and
226 oxido-reduction reactions, in addition to the formation of secondary minerals and clay minerals.



227 The clay fraction is defined as a solid solution made up of a combination of pure clay end-
228 members. The clay solid solution has a composition that changes over time, reflecting the
229 impurity of the precipitating clays during low-temperature water-rock interactions (Tardy and
230 Fritz, 1981). The KIRMAT code has already been applied in geochemical modeling of alluvial
231 groundwaters (Lucas et al., 2010) and surface waters (Lucas et al., 2017; Ackerer et al., 2018).
232 For this study, the modeling strategy is adapted from Ackerer et al. (2018) to consider the new
233 transit time and water mixing constrains provided by the hydrological code NIHM. To capture
234 the chemical composition of the spring and the piezometer waters, numerical simulations were
235 performed along the flow lines that were determined through the backtracking approach. A
236 sketch of the hydrogeochemical modeling strategy is provided in figure 5. For each flow line,
237 several KIRMAT simulations were performed with different starting positions along the active
238 part of the line. The starting positions represent the locations at which the soil solutions
239 percolate through the subsurface shallow aquifer. These variable starting positions are spaced
240 with a constant distance along the flow line. The soil solutions collected in the south at the
241 beech site (HP) and in the north at the spruce site (VP) were considered representative of the
242 soil solutions for the southern and northern parts of the catchment, respectively. The data of
243 soil solution chemistry used in this study are available in Prunier et al. (2015). Data related to
244 the bedrock properties, such as the mineralogical compositions, the mineral reactive surfaces
245 and the kinetic constants of the dissolution reactions, are given in Ackerer et al. (2018). By
246 following this modeling strategy, the simulations that consider soil solutions percolating at the
247 upper part of the catchment reflect the chemical evolution of waters with long path lengths and
248 long transit times within the aquifer. By contrast, shorter path lengths and shorter transit times



249 are associated with the percolation of soil solutions that occurs in the vicinity of the sampling
250 locations (figure 5). Because the springs or the piezometers collect waters from different origins
251 and with contrasted transit times, integration along each water flow line was performed. The
252 aim of the integration is to determine the mean chemical composition resulting from the mixing
253 of the waters characterized by variable transit times (figure 5). The integrated chemical
254 composition of the waters provided by a given flow line is calculated by taking the arithmetic
255 mean of the solute concentrations calculated by the succession of the KIRMAT simulations along
256 the flow line (figure 5). This arithmetic mean reflects a simple full mixing of uniform water fluxes
257 irrespective of their short or long transit times. In other words, the soil solutions are assumed to
258 percolate uniformly within the aquifer and are then conveyed along the slopes by uniformly
259 distributed mass of water until reaching the sampling locations.

260 **4- Hydrological modeling results**

261 **4-1 Spatial variability of the flow lines**

262 The results provided by the hydrological code NIHM show that to first order, the Strengbach
263 catchment is well drained and that the topography exerts an important control on the flow line
264 distribution (figure 4). Along the hillsides presenting linear or slightly convex slopes, the water
265 flow lines present simple characteristics. The flow paths are nearly parallel, and the water
266 velocities are similar along the different flow lines on this type of hillside. The water velocities
267 tend to increase when moving downstream (longer traveled distances for a given transit
268 duration, see Fig. 4), with slower velocities near the main crests and higher velocities on the
269 steepest parts of the hillsides. The waters collected along this type of hillside are therefore



270 characterized by small variability of transit times. This is the case for the CS1, CS3 and RH3
271 spring waters located on the southern and northern parts of the catchment (figure 4). This is
272 also the case for the piezometers PZ3 and PZ5 in the southern part of the watershed (figure 4).
273 For the samplings located on linear or slightly convex slopes (CS1, CS3, RH3, PZ3 and PZ5), the
274 characteristics of the different flow lines that feed each site are therefore comparable for a
275 given site and for a given date. By contrast, in the vicinity of the valley and in the topographic
276 depressions, the hydrological modeling indicates that the flow line characteristics are more
277 variable. Because flow lines coming from different hill-sides can feed a topographic depression,
278 mixing of different flow lines with variable flow paths and contrasting water velocities can occur
279 at these locations. The waters collected in valleys or in topographic depressions are therefore
280 characterized by a higher variability of transit times. This is the case for the CS2 and CS4 springs,
281 which are located in a depression in the axe of the small valley and surrounded by slopes with
282 various orientations and a complex flow line distribution (figure 4). For these two springs, the
283 characteristics of the different flow lines can be different for a given date.

284 **4-2 Temporal variability of the flow lines**

285 Hydrological modeling under general transient conditions can render the evolution over time of
286 water flows in the Strengbach watershed but also of other hydraulic variables or parameters. As
287 an example, after an important rainfall event (30/03/2010 in Fig. 6), snapshots of the average
288 hydraulic conductivity in the subsurface show increasing values with decreasing elevation in the
289 watershed. The same observation holds for hydraulic conductivity during drought periods (see
290 29/11/2011, in Fig. 6). Provided that the hydraulic head gradient is largely dominated by the
291 topography and therefore almost constant over time (Fig. 6), the water velocities are increasing



292 along the flow lines from crests to valleys, irrespective of the wet versus dry hydrological
293 periods. For the CS1 spring, the mean flow velocities along the flow lines vary from
294 approximately 1 m/day to 7 m/day between the severe drought of 29/11/2011 and the strong
295 flood of 30/03/2010 (figure 7). For the same dates, the mean velocities vary from 2 – 12 m/day,
296 1 – 4 m/day and 1 – 9 m/day for the springs CS2, CS3 and CS4, respectively. The variations from
297 drought to flood are very similar for the piezometer waters, with velocities in the ranges 2 – 10
298 m/day and 2 – 12 m/day for the PZ3 and PZ5 piezometers, respectively. The RH3 spring located
299 on a steeper part of the northern slopes exhibits flow velocity variations from 5 to 20 m/day
300 from dry to flood conditions. In addition to the flow velocity variations, the hydrological
301 simulations also reveal variability in the lengths of the active parts of the flow lines. Such
302 variability is triggered by the particular seasonal variations of the hydraulic conductivities within
303 the catchment. During periods of drought, the simulations indicate a strong decrease of
304 hydraulic conductivities close to the main crests and much smaller variations at mid-slopes
305 (figure 6). The crests rapidly dry out, whereas the areas at mid-slopes still supply some water to
306 the stream network. These contrasting hydrological behaviors result from the differences in
307 aquifer thickness and water storage between the crests and the other parts of the catchment
308 (figure 2). Thin aquifer, flow divergence and absence of feeding areas prevent large water
309 storage on the crests, in opposition to mid-slope parts with much thicker aquifers and the
310 presence of feeding areas upstream. This particular pattern simulated for the hydraulic
311 conductivities implies that the active parts of the flow lines extend up the main crests during
312 important floods, whereas they are limited to mid-slopes after a long dry period. The
313 consequence of this hydrological functioning is to moderate the seasonal variations of the



314 transit times of waters, as the active lengths of flow lines vary simultaneously with water flow
315 rates. Calculations indicate that for the spring and piezometer waters collected in this study, the
316 mean transit times of waters only vary from approximately 1.75 to 4 months between the
317 strongest flood and the driest conditions.

318 **5- Hydrogeochemical modeling results**

319 Modeling the geochemical composition of waters from the different springs and piezometers
320 selected for this study was performed following the procedure described in paragraph 3-2. The
321 results are presented below by grouping sources and piezometers according to their
322 hydrogeological characteristics.

323 **5-1 CS1 and CS3 springs (southern slope)**

324 The CS1 and CS3 springs emerge on the same slope and drain the same rocks. Their hydrological
325 behavior is also very similar in terms of flow lines and water transit times. The interesting
326 consequence of the simple flow line distribution for these springs is that a single flow line can be
327 considered as representative of all the flow lines that are feeding the spring, irrespective of the
328 hydrological conditions. Hydrogeochemical simulations were performed along a single flow line
329 for different hydrological periods using the methodology illustrated in figure 5. The case of CS1
330 spring is used below to highlight the main results obtained from this approach. For the strong
331 flood of 30/03/2010, the KIRMAT simulations modeling the waters coming from the proximity of
332 the spring and characterized by short transit times produced too much diluted solutions,
333 whereas the waters coming from the main crests are too much concentrated to reproduce the
334 spring water chemical composition. However, after an integration of all the waters arriving at



335 CS1 with the different transit times employed for the simulation, the resulting geochemical
336 composition correctly reproduces the chemical composition of CS1 spring water at this date
337 (H_4SiO_4 , Na^+ , K^+ , Mg^{2+} , and Ca^{2+} concentrations, figure 7). A similar conclusion is obtained for the
338 important drought of 29/11/2011. Again, geochemical integration of all the waters arriving at
339 CS1 along a water line but with different transit times correctly reproduces the chemical
340 composition of the CS1 spring waters collected on this date (figure 7). This is actually the case
341 regardless of the time period considered. The coupled hydrological and hydrogeochemical
342 approach has been applied for the CS1 spring for 6 dates covering the whole range of the water
343 discharges of the spring (tables 1). The modeling results show that the seasonal variations of the
344 water chemical composition of the CS1 spring over the whole range of observed flow rates at
345 CS1 (figure 8). Simulations especially account for the 20-30% variation in H_4SiO_4 concentrations,
346 the 10-20% variation in Na^+ concentrations, and the relatively stability of the pH of the CS1
347 waters (figure 8). Similar results are obtained for the CS3 spring (EA1), showing, as for the CS1
348 spring, that the proposed modeling approach is able to correctly capture the water chemical
349 composition of the CS3 spring.

350 **5-2 PZ3 and PZ5 piezometers (southern slope)**

351 The two piezometers PZ3 and PZ5 are located on the southern part of the catchment, and their
352 waters drain granitic bedrock similar to that drained by the CS sources. As for the CS1 and CS3
353 springs, the NIHM modeling results show that the flow lines arriving at the PZ3 piezometer are
354 characterized by a relatively simple distribution. The flow lines are close to each other, and they
355 render similar water velocities on the slopes (figure 4). For the PZ5 piezometer located
356 downstream, the flow lines cover a larger area on the slope, especially during droughts (figure



357 4). However, for a given date, all the flow lines show similar velocities, with particularly fast
358 flows on a lower portion of the hillslope. These results imply that, as for the CS1 and CS3
359 springs, the hydrogeochemical simulations of PZ3 and PZ5 piezometer waters can be performed
360 by relying upon a single flow line representative of all the waters collected by the piezometers
361 on a given date. The geochemical integration along the flow line has been performed in the
362 same manner as detailed above, and this approach is able to reproduce the chemical
363 composition of the waters of the two piezometers, as illustrated in figure 9 for the flood of the
364 05/05/2015 and in EA2 for the dry conditions of 10/11/2015. For the CS1 and CS3 springs, the
365 results also point to a modest variability of the solute concentrations over changing hydrological
366 conditions (not shown). Together, these modeling results show that the linear or slightly convex
367 slopes on the southern part of the catchment allow to correctly capture the water chemistry of
368 each sampling site with a straightforward integration along a single and representative flow line.

369 **5-3 The CS2 and CS4 springs (in the valley axe)**

370 CS2 and CS4 spring waters drain the same granitic bedrock as the CS1 and CS3 waters, but are
371 located in the axe/along the direction of the small valley of the Strengbach stream and
372 surrounded by slopes of various orientations and inclinations (figure 4). Consequently, the
373 distribution of the flow lines is much more scattered than for the CS1 and CS3 springs. The
374 modeling strategy applied for these two springs and the results are detailed below for the CS2
375 spring. For this spring, and for all the hydrological conditions, two different groups of flow lines
376 have been determined by the backtracking approach: a northern group characterized by
377 relatively slow velocities and a southern group with higher velocities (figure 4). When the
378 hydrological conditions vary from a strong flood (30/03/2010) to an important drought



379 (29/11/2011), the flow rates tend to decrease along all the flow lines (figure 10). For example,
380 the mean flow velocities along the flow lines vary from approximately 12 m/day to 2 m/day
381 between these two dates. However, for a given date, the northern group systematically renders
382 slower velocities than the southern group. This scattered distribution of the flow lines implies
383 that a single specific flow line cannot be representative of all the waters collected by the spring.
384 The flow lines calculated using the NIHM model allow for constraining the trajectories of the
385 waters within the watershed; however, the simulations performed in this study cannot provide
386 the mass fluxes of water carried by each flow line. Consequently, a straightforward calculation
387 of the chemistry of the CS2 spring, such as detailed above for CS1, is not applicable because the
388 mixing proportions between the different flow lines are unknown. Alternatively, it is possible to
389 determine the concentrations in the waters carried by the slowest and the fastest flow lines
390 that are feeding the spring and to compare the results with the observed chemistry of the
391 spring water. The results indicate that for all the hydrological conditions, the concentrations
392 calculated from the geochemical integration along the slowest and the fastest flow lines are
393 able to correctly frame the chemical composition in terms of H_4SiO_4 , Na^+ , K^+ , Mg^{2+} , and Ca^{2+} of
394 the CS2 spring waters (figure 10). The observed chemistry of the CS2 spring is bounded by the
395 chemical compositions of the waters carried by the slowest and fastest flow lines. The modeling
396 results also suggest that the contributions of the slow and fast flow lines are comparable over
397 most of the hydrological conditions, as the observed concentrations are in general at the
398 midpoint between the min (i.e., fast) and max (i.e., slow) boundaries (see Fig. 10). It is only for
399 the important droughts that the spring chemistry seems to be mainly controlled by the southern
400 and faster group of flow lines. Further works to precisely estimate the mass fluxes of water



401 carried by each flow line are necessary to calculate the chemistry of the CS2 spring water with a
402 weighted mixing calculation. The same conclusions apply to the CS4 spring located in the
403 proximity of CS2 spring.

404 **5-4 The RH3 spring (northern slope)**

405 The RH3 spring is located on the northern part of the catchment (figure 4), where steep slopes
406 imply fast water velocities and subparallel flow lines. However, if the distribution of the flow
407 lines on the RH3 hillside is simple (as for the CS1 and CS3 springs) the precise lithological nature
408 of the bedrock drained by the RH3 waters is more difficult to constrain (see also Ackerer et al.,
409 2018). Unlike the southern slope, the bedrock of the northern part of the catchment exhibits a
410 complex lithology, with gneiss outcropping in the upper part of the slope and granite of variable
411 degree of hydrothermal overprinting in the intermediate and lower parts. These lithological
412 variations can explain the differences in chemical composition between the RH3 spring waters
413 and the waters of the southern part of the catchment: the RH3 spring waters are characterized
414 by systematically higher concentrations of K^+ and Mg^{2+} cations but show similar concentrations
415 for the other major elements (Ackerer et al., 2018; Pierret et al., 2014). The vertical extension of
416 the gneiss and the spatial variability of the hydrothermal overprinting on the northern slopes
417 are not very well known. It is therefore difficult to determine the exact lithology that is
418 percolated by the flow lines feeding the RH3 spring. A straightforward modeling of the RH3
419 spring waters, such as that performed for the CS1 and CS3 sources, is thus not possible.
420 Alternatively, simulations of two extreme cases can be performed by assuming that the flow
421 lines only run, either on gneiss or on hydrothermally altered granite. When only considering the
422 hydrothermally altered granite, the simulated concentrations of H_4SiO_4 and Na^+ are close to the



423 measured ones. However, the concentrations of K^+ and especially Mg^{2+} are clearly
424 underestimated (figure 11). In the case of the flow lines only running on gneiss, the simulated
425 concentrations of H_4SiO_4 and Na^+ also match the data. However, due to the higher abundance of
426 biotite in the gneiss, the simulated concentrations of K^+ and Mg^{2+} are much higher than the
427 measured ones (figure 11). At this stage, it is therefore reasonable to propose that the chemical
428 composition of the RH3 spring waters reflects mixing of the two lithological influences. By
429 assuming a geochemical conservative mixing, which is likely a too simplistic scenario, the results
430 would indicate that the flow lines portions running on gneiss and on hydrothermally altered
431 granite count for approximately 40-50% and 50-60% of the total water path length, respectively.
432 Further works to estimate the location of the contact between gneiss and granite are required
433 for more realistic modeling and hence a deeper interpretation of the chemical composition of
434 RH3 spring waters. In any case, the important point to stress here based on the above
435 simulations is that the complex lithology and bedrock heterogeneity mainly impact the K^+ and
436 the Mg^{2+} budget of the RH3 waters, but not or only slightly the H_4SiO_4 and Na^+ concentrations,
437 which control the main part of global weathering fluxes carried by the Strengbach spring waters.
438 These results readily explain why although the RH3 spring waters exhibits higher Mg^{2+} and K^+
439 concentrations than the other CS springs, they carry relatively similar global weathering fluxes
440 (Viville et al., 2012; Ackerer et al., 2018).

441 **6- Discussion**

442 The modeling approach proposed in this study and based on the coupling of the NIHM and
443 KIRMAT codes, allows for building a better modeling scheme than those commonly used in
444 previous studies regarding the hydrogeochemical modeling of surface waters at the watershed



445 scale. In such previous works, the geochemical simulations were performed mainly along a
446 single 1D flow line, only characterized by homogeneous mean hydrological properties (Goddéris
447 et al., 2006; Maher et al., 2011; Moore et al., 2012; Lucas et al., 2017; Ackerer et al., 2018). In
448 the previous study on the Strengbach watershed (Ackerer et al., 2018), the soil solutions were
449 also assumed to percolate in the bedrock only at a single starting point of the flow lines.
450 Although these previous approaches were useful for determining the long-term evolution of
451 regolith profiles and/or the mean chemistry of waters at the pluri-annual scale, they cannot be
452 used to discuss the seasonal variations of the water chemical composition. The NIHM-KIRMAT
453 coupling approach makes this possible, as it provides the spatial distribution of the flow lines at
454 the watershed scale and their variations over time. Furthermore, the proposed modeling
455 approach also integrates a soil solution percolation scheme with inlets uniformly distributed along
456 the slope, which is more realistic than a scheme assuming that each sampled site is fed by a
457 single flow line carrying waters with a unique transit time. The consistency of the modeling
458 results with the measured concentrations over the whole range of the hydrological conditions
459 certainly gives weight to the application of the proposed modeling approach to the Strengbach
460 catchment. Such consistency also gives weight to the assumptions made regarding the modeling
461 parameters used in this work, i.e., reactive surfaces and kinetic constants. It also gives weight to
462 the conclusions and implications that can be deduced regarding the hydrogeochemical
463 functioning of the watershed, and the origin of the chemostatic character of these waters.
464 These different points are detailed below.

465 **6-1 Choices of the reactive surfaces and the kinetic constants**



466 For the geochemical simulations performed in this study, the kinetic constants that were used
467 to describe the dissolution reactions of the primary minerals are standard constants determined
468 through laboratory experiments. The reactive surfaces of the primary minerals were calculated
469 by assuming a simple spherical geometry for all the minerals, and the mean size of the minerals
470 was estimated from thin section observations of the bedrock samples. Such choices can appear
471 surprising as over the last years, several studies have suggested that the kinetic constants
472 determined through laboratory experiments overestimate the rates of the dissolution reactions
473 in natural environments (White and Brantley, 2003; Zhu, 2005; Moore et al., 2012; Fischer et al.,
474 2014). The origin of this laboratory-field discrepancy is still a matter of debate (Fischer et al.,
475 2014). Different processes have been proposed to explain the gap between laboratory and field
476 estimates, such as the crystallographic anisotropy (Pollet-Villard et al., 2016), progressive
477 occlusion of the primary minerals by clays (White and Brantley, 2003), or the formation of
478 passivation layers at the surfaces of the minerals (Wild et al., 2016, Daval et al., 2018). The
479 difficulty to reconcile field and laboratory estimates can also be related to the challenge of
480 defining relevant reactive surfaces at different space scales (Li et al., 2006; Navarre-Sitchler and
481 Brantley, 2007). The present modeling work regarding the Strengbach catchment shows that
482 the chemical composition variability of the spring and piezometer waters is fully captured via
483 geometric reactive surfaces and standard kinetic constants, while respecting the water-rock
484 interaction times within the catchment. This result suggests that the mean rates of the
485 weathering reactions employed in this modeling work are realistic, which in turn implies that
486 the modeling approach developed in this study does not underline significant mismatches
487 between field and laboratory reaction rates. More details are given in the following to



488 investigate why geometric reactive surfaces and standard kinetic constants are able to correctly
489 capture the water chemistry. The calculated rates of the dissolution reactions depend on the
490 product between the kinetic constants of the reactions and the mineral reactive surfaces. In the
491 experimental studies performed for determining the kinetic constants of dissolution reactions,
492 the constants are usually determined by normalizing the experimental weathering rates with
493 the Brunauer-Emmett-Teller surfaces determined from experiments of gas absorption (BET
494 surfaces; Chou and Wollast, 1986; Lundstrom and Ohman, 1990; Acker and Bricker, 1992;
495 Amrhein and Suarez, 1992; Berger et al., 1994; Guidry and Mackenzie, 2003). In table 2, the BET
496 surfaces are compared with the geometric surfaces of the minerals involved in the dissolution
497 experiments, recalculated from the size ranges of the minerals. For most of the minerals
498 (apatite, quartz, albite, K-feldspar, and anorthite), the geometric surfaces are within the same
499 order of magnitude as the BET surfaces, even if often slightly lower (table 2). However, as the
500 BET surfaces are determined with fairly large uncertainties, especially for low BET surfaces (up
501 to $\pm 70\%$), and as they can be very different depending on the gas used (up to 50% of difference
502 between N₂ or Kr absorption; Brantley and Mellott, 2000), the above differences between the
503 geometrical and the BET surfaces cannot be considered significant for the majority of minerals
504 used in the Strengbach simulations. A significant difference only appears for biotite, with the
505 geometric surfaces one order of magnitude less than the BET surfaces (table 2). However, for
506 biotite, due to its layered structure, it has been shown that approximately 80 – 90% of the
507 surface area accessible by the gases used to estimate BET surfaces is not accessible for
508 weathering reactions (Nagy, 1995). In the case of biotite, the effective surface area for the
509 water-rock interactions would thus be, in a rather fortuitous manner, a surface area close to the



510 geometric one. The above considerations and observations thus explain why for a granitic
511 bedrock as found in the Strengbach catchment, the geometric surfaces are relevant to describe
512 the surfaces of water-rock interactions at the space and time scales of this study. An immediate
513 corollary is that the values of the standard kinetic constants are also appropriate to calculate
514 reaction rates with mineral geometric surfaces in our modeling approach. This ability may be
515 related to the fact that all the minerals that have been used in the dissolution experiments and
516 in the kinetic studies were collected in the field (e.g., Acker and Bricker, 1992; Amrhein and
517 Suarez, 1992). These minerals were likely affected by anisotropy, passivation layers, and any
518 types of aging effects related to long-term water-rock interactions. Our results might therefore
519 mean that the standard kinetic constants obtained in such experiments integrate the aging
520 effects that have affected the reactivity of the primary minerals in natural environments. This
521 would explain why it is possible to capture the full variability of the water chemistry in an
522 elemental catchment with simple geometric reactive surfaces and standard kinetic constants. It
523 is important to emphasize at this stage that the results of our simulation strengthen the idea
524 that the low surfaces calculated from the geometrical shapes of minerals provide good
525 estimates of the reactive surfaces within the natural environment (Brantley and Mellott, 2000;
526 Gautier et al., 2001; White and Brantley, 2003; Zhu, 2005; Li et al., 2017). They are certainly the
527 values to be used for hydrogeochemical modeling such as that performed in this work, in
528 addition to the use of the experimental kinetic constants for mineral dissolution. These
529 conclusions are certainly not specific to the Strengbach catchment and could be applicable to
530 many other granitic catchments.

531 **6-2 Implications for the acquisition of the water chemistry**



532 The results of the NIHM-KIRMAT hydrogeochemical modeling have strong implications
533 regarding the hydrogeochemical functioning of the Strengbach watershed. The NIHM modeling
534 shows that the hydrological functioning of the watershed is correctly simulated by water
535 circulations in the shallow subsurface, i.e., in a saprolitic aquifer. No contribution of waters
536 circulating in the deep fracture network of the granitic bedrock and observed during the drilling
537 campaigns is necessary. The deep-water circulation pathways are probably disconnected from
538 the shallow subsurface, or with mean hydraulic heads less than those of the subsurface, at least
539 at the Strengbach catchment scale, and does not significantly impact the water budget of the
540 Strengbach catchment. As detailed in section 4-1, the modeling results show that water in the
541 shallow aquifer flows along streamlines with fairly simple geometries. At the scale of the
542 watershed (figure 4), the geometry of the flow lines validates the hypothesis built on the basis
543 of the geochemical and Sr-U isotopic data that the spring waters of these mid-mountain basins
544 (i.e., the Strengbach and Ringelbach watersheds; Schaffhauser et al., 2014; Pierret et al., 2014)
545 are supplied by waters from distinct flow paths without real interconnections. More
546 importantly, the modeling results emphasize the importance of water transit times within the
547 watershed as a main feature controlling the chemical composition of subsurface waters at the
548 Strengbach catchment. Along all the slopes, the waters coming from the proximity of the crests
549 and characterized by a long transit time systematically render higher concentrations than the
550 waters with shorter pathways and transit times. When the hydrological conditions change from
551 wet to dry periods, the solute concentrations also tend to increase with the increase in the
552 mean transit time of waters. Our results demonstrate in particular that for the CS1 and CS3
553 sources and for the PZ3 and PZ5 piezometers, all located on the southern slope of the



554 watershed, over a homogeneous granitic bedrock, and all characterized by flow lines of fairly
555 simple geometries (section 4), the spatial and temporal variations of their geochemical
556 composition are fully explained by differences in water residence times. Residence time
557 variations between high and low discharge periods explain the temporal variations of
558 geochemical signatures within each site, and the differences in mean residence times of waters
559 supplying the different sources and piezometers explain the various chemical compositions
560 between the different sites. Only the CS2 and CS4 springs, located in a depression, are supplied
561 by two different types of water flow lines, the contribution of which could change over time.
562 However, the mixing of different flow lines has probably a relatively modest impact, and at the
563 scale of the watershed, the results show that the duration of water-rock interaction exerts a
564 first-order control on the chemical composition of waters, in addition to the lithological
565 parameter. This study brings also strong constraints on the spatial repartition of the weathering
566 processes. For the modeling strategy developed in this study, the chemical composition of the
567 spring and piezometer waters are calculated by integrating the chemical composition of waters
568 introduced at different starting positions along the active part of the flow lines (figure 5). In
569 each of the simulations, a fixed distance between the initial positions of the KIRMAT simulations
570 along the flow lines was used. The modeling results show that through the geochemical
571 integration, the concentrated waters coming from the main crests are naturally
572 counterbalanced by the diluted waters infiltrating close to the sampling sites. From flood to
573 drought events, the mean transit times are obviously impacted by the variable velocities along
574 the flow lines, but regardless of the hydrological conditions, it is always possible to explain the
575 water chemistry of the sampling sites with the above integration scheme. Such repeatable



576 consistency between data and simulations indicates that this circulation scheme is certainly
577 quite realistic for the Strengbach catchment. In other words, this scheme supports the idea
578 suggested in Ackerer et al. (2016) that at the scale of the watershed, the solute chemistry is
579 acquired through reactions and weathering processes that are spatially relatively homogenous
580 within the watershed.

581 **6-3- Origin of the chemostatic behavior in the Strengbach catchment**

582 The hydrogeochemical monitoring of the spring, piezometer, and stream waters performed in
583 the Strengbach catchment clearly shows that this catchment has a chemostatic behavior (e.g.,
584 Viville et al., 2012; Ackerer et al., 2018; this study). All the spring and the piezometer waters
585 have chemical concentrations impacted by changes in the hydrological conditions, but the
586 concentration variation ranges are by far narrower than variation ranges of water discharges,
587 which define the chemostatic behavior of a hydrological system. For the waters exhibiting the
588 largest concentration variations (spring CS1), there is a modest increase of approximately 10-
589 30% in the concentrations of H_4SiO_4 and Na^+ from floods to severe drought events, while ~~at the~~
590 ~~same time~~, the water discharges may vary by a factor of 15 (figure 7). This modest variability of
591 the solute concentrations over a wide range of water discharges is not specific to the
592 Strengbach catchment; it has rather been observed in several watersheds spanning different
593 climates and hydrological contexts (Godsey et al., 2009; Clow and Mast, 2010; Kim et al., 2017).
594 Different origins for the chemostatic behavior have been proposed, such as a modification of
595 the mineral reactive surfaces during changing hydrological conditions (Clow and Mast, 2010), a
596 small concentration difference between slow and fast moving waters (Kim et al., 2017), or the
597 fact of reaching an equilibrium concentration along the water pathway (Maher, 2010). To date,



598 the study of concentration-discharge relationships has been intensively used to assess the
599 chemostatic behavior of waters (Godsey et al., 2009; Kim et al., 2017; Ameli et al., 2017).
600 However, the lack of precise knowledge regarding the water transit times limits our ability to
601 clearly discuss the origin of the chemostatic behavior on the single basis of the concentration-
602 discharge relationships. The coupled approach presented in this study offers a renewed
603 opportunity to discuss the origin of the chemostatic behavior in catchments because the
604 acquisition and the evolution of the water chemistry can be simulated along flow lines that have
605 been independently determined via timely and spatially distributed hydrological modeling.

606 The results from the hydrological model show that the characteristics of the flow lines are
607 affected by the changes in the hydrological conditions. After important precipitations, high
608 water contents and large hydraulic conductivities (as the local mean value integrated over the
609 aquifer thickness including the vadose and saturated zones) are simulated in the vicinity of the
610 crests and all along the small valley of the catchment (figure 6). During drought periods, the
611 crest lines have progressively dried out, and the hydraulic conductivities strongly decrease on
612 the upper parts of the watershed. Only some locations at mid-slopes and along the direction of
613 the principal valley exhibit modest hydraulic conductivities (figure 6). This response of the
614 hydraulic conductivities implies that during floods, the water velocity significantly increases
615 along the flow lines, but the length of the active parts of the flow lines also increase as waters
616 collected downstream may also come from the neighborhood of the main crests. During
617 drought periods, the water velocity is slower, but the length of the active parts of the flow lines
618 also tends to decrease, as the waters are principally supplied by mid-slope areas characterized
619 by a thicker aquifer. For illustration, and for the CS1 spring, the water velocities varied along the



620 flow lines between 7 and 0.5 m/day during the flood of 30/03/2010 and were approximately
621 0.5-1 m/day during the important drought of the 29/11/2011 (figure 6). At the same time, the
622 active parts of the flow lines were reduced from 160 m to 110 m from the flood to the drought
623 events (figure 7). This hydrological functioning implies that the water velocities along the flow
624 lines and the active lengths of the flow lines vary in opposite manners from drought to flood
625 events. This hydrological behavior buffers the variations of the water transit times over
626 changing hydrological conditions and explains why the mean transit times span much narrower
627 variation ranges than the discharges of water at the collected springs. For example, the
628 calculated mean transit times of waters for the CS1 spring vary from 1.75 to 3.13 months
629 between the strongest flood and the driest period that have been studied, whereas the water
630 discharges vary from 1.523 L/s to 0.098 L/s (figure 7). Because the time of the water-rock
631 interactions exerts a first-order control on the chemical composition of waters, the modest
632 variability of the mean transit times is directly responsible for the relative stability of the
633 chemical composition of waters within the catchment.

634 It is important to be reminded that no modifications of the reactive surfaces and of the
635 dissolution kinetic constants were necessary to reproduce the seasonal variability of the water
636 chemistry. It is also important to emphasize that the simulated chemical compositions of waters
637 remain far from a state of chemical equilibrium with respect to primary minerals. The calculated
638 Gibbs free energy for the primary minerals ranges from -120 to -100 kJ/mol for apatite, -90 to -
639 80 kJ/mol for biotite and anorthite and -30 to -20 kJ/mol for albite and K-feldspar. These far-
640 from-equilibrium values for the Gibbs free energy imply that the reaction rates calculated using
641 hydrogeochemical codes such as KIRMAT, which are based on the transient state theory (TST;



642 Eyring, 1935), are realistic for most of the primary minerals in this type of hydrological context.
643 Regarding the simulations performed in this study, the relatively short residence times of waters
644 and the precipitation of clay minerals prevent reaching a state of chemical equilibrium between
645 waters and primary minerals. The results also indicate that a clay solid solution is a relevant
646 method to capture the clay dynamic in this type of watershed and that a clay solid solution
647 precipitated in thermodynamic equilibrium is able to generate realistic clay precipitation rates
648 and reliable water chemistry (Ackerer et al., 2018; this study). A more precise approach of the
649 formation of clay phases would request to simulate a kinetically-controlled nucleation and
650 growth of clay particles: it is clear that such complex phases are probably produced in
651 oversaturation state as can be described using the numerical code NANOKIN (Fritz et al., 2009,
652 Noguera et al. , 2011). However, the results obtained here show that equilibrium condition for
653 clay formation is a reasonable first approximation for predicting clay production. Taken
654 together, these results show that the solute concentrations are not limited by a chemical
655 equilibrium; they simply are weakly variable over time because of the short and moderately
656 variable water residence times in the watershed. The chemostatic behavior of the surface and
657 the shallow subsurface waters is therefore only due to a strong hydrological control of the
658 water transit times within the watershed. This conclusion can most likely be extended to the
659 other mountainous watersheds of this type, in which water pathways and transit times are
660 mainly controlled by gravity driven flow along steep slopes.

661 **7- Conclusion**

662 This study demonstrates the potential of coupling physically based and distributed hydrological
663 modeling with hydrogeochemical modeling as a way to better understand variability over time



664 and space of the composition of surface and subsurface waters. The independent estimation of
665 the water transit times provided by hydrological simulations is a clear added value to constrain
666 the geochemical modeling approaches. This study shows that the durations of water-rock
667 interactions exert a first-order control on the chemical composition of waters and that the
668 acquisition of the water chemistry can be explained by weathering processes that are spatially
669 fairly homogeneous over the catchment. The hydrological functioning of the watershed also
670 indicates that the chemostatic behavior of the water chemistry is a direct consequence of the
671 strong control exerted by hydrological processes on water transit times. In the present case, The
672 variations in flow lines distributions from drought to flood events result in a modest seasonal
673 variability of mean water transit times, which in turn explains the relative stability of the solute
674 concentrations in waters. The consistency between measured and modeled concentrations
675 while respecting the water-rock interaction times provided by the hydrological simulations
676 shows that it is possible to capture the chemical composition of waters with simply determined
677 reactive surfaces and standard kinetic constants. The results of our simulations strengthen the
678 idea that the low surfaces calculated from the geometrical shapes of minerals are a good
679 estimate of the reactive surfaces within the natural environment and certainly the values to be
680 used for hydrogeochemical modeling such as that performed in this work, in addition to the use
681 of the experimental kinetic constants for mineral dissolution. Overall, this work shows that the
682 hydrogeochemical functioning of an elementary watershed such as the Strengbach catchment is
683 relatively simple. It is possible to correctly assess the variability of the chemical composition of
684 waters through process-based modeling approaches and by only formulating few simple
685 hypotheses regarding the functioning of the watershed.



686

687 **Acknowledgements:** This work and the Julien Ackerer's salary were financially supported by the

688 French ANR Program (Project CANTARE- Alsace) under grant agreement ANR-15-CE06-0014.

689 This work also benefited from fruitful discussions with D. Daval.

690



691 **Bibliography**

692 Acker, J. G. and Bricker, O. P.: The influence of pH on biotite dissolution and alteration kinetics at low
693 temperature. *Geochim. Cosmochim. Acta*, 56(8), 3073-3092, 1992.

694 Ackerer, J., Chabaux, F., Van der Woerd, J., Viville, D., Pelt, E., Kali, E., Lerouge, C., Ackerer, P., Di Chiara
695 Roupert, R. and Négrel, P.: Regolith evolution on the millennial timescale from combined U–Th–
696 Ra isotopes and in situ cosmogenic ¹⁰Be analysis in a weathering profile (Strengbach catchment,
697 France). *Earth Planet. Sci. Lett.*, 453, 33-43, 2016.

698 Ackerer, J., Chabaux, F., Lucas, Y., Clément, A., Fritz, B., Beaulieu, E Viville D., Pierret, M.C., Gangloff, S.
699 and Négrel, P.: Monitoring and reactive-transport modeling of the spatial and temporal
700 variations of the Strengbach spring hydrochemistry. *Geochim. Cosmochim. Acta*, 225, 17-35,
701 2018.

702 Ameli, A. A., Beven, K., Erlandsson, M., Creed, I. F., McDonnell, J. J. and Bishop, K.: Primary weathering
703 rates, water transit times, and concentration-discharge relations: A theoretical analysis for the
704 critical zone. *Water Resour. Res.*, 53, 942-960, 2017.

705 Amrhein, C. and Suarez, D. L.: Some factors affecting the dissolution kinetics of anorthite at 25 C,
706 *Geochim. Cosmochim. Acta*, 56, 1815-1826, 1992.

707 Beaulieu, E., Goddérís, Y., Donnadiou, Y., Labat, D. and Roelandt, C.: High sensitivity of the continental-
708 weathering carbon dioxide sink to future climate change, *Nature Climate Change*, 2, 346, 2012.

709 Beaulieu, E., Lucas, Y., Viville, D., Chabaux, F., Ackerer, P., Goddérís, Y. and Pierret, M. C. : Hydrological
710 and vegetation response to climate change in a forested mountainous catchment, *Modeling
711 Earth Systems and Environment*, 2, 191, 2016.

712 Berger, G., Cadore, E., Schott, J. and Dove, P. M.: Dissolution rate of quartz in lead and sodium
713 electrolyte solutions between 25 and 300 C: Effect of the nature of surface complexes and
714 reaction affinity, *Geochim. Cosmochim. Acta*, 58, 541-551, 1994.



- 715 Brantley, S. L. and Mellott, N. P.: Surface area and porosity of primary silicate minerals, *Am. Mineral.*, *85*,
716 1767-1783, 2000.
- 717 Camporese, M., Paniconi, C., Putti, M. and Orlandini, S.: Surface-subsurface flow modeling with path-
718 based runoff routing, boundary condition-based coupling, and assimilation of multisource
719 observation data, *Water Resour. Res.* *46*, W02512, [doi:10.1029/2008WR007536](https://doi.org/10.1029/2008WR007536), 2010.
- 720 Chabaux, F., Viville, D., Lucas, Y., Ackerer, J., Ranchoux, C., Bosia, C., Pierret, M.C., Labasque, T., Aquilina,
721 L., Wyns, R., Lerouge, C., Dezaye, C. and Négrel, P.: Geochemical tracing and modeling of surface
722 and deep water–rock interactions in elementary granitic watersheds (Strengbach and Ringelbach
723 CZOs, France), *Acta Geochim.*, *36*, 363-366, 2017.
- 724 Chou, L., and Wollast, R.: Steady-state kinetics and dissolution mechanisms of albite. *Am. J. Science*, *285*,
725 963-993, 1985.
- 726 Clow, D. W. and Mast, M. A.: Mechanisms for chemostatic behavior in catchments: implications for CO₂
727 consumption by mineral weathering, *Chem. Geol.*, *269*, 40-51, 2010.
- 728 Daval, D., Calvaruso, C., Guyot, F. and Turpault, M. P.: Time-dependent feldspar dissolution rates
729 resulting from surface passivation: Experimental evidence and geochemical implications. *Earth*
730 *Planet. Sci. Lett.*, *498*, 226-236, 2018.
- 731 Ebel, B. A. and Loague, K.: Physics-based hydrologic-response simulation: Seeing through the fog of
732 equifinality. *Hydrological Processes: An International Journal*, *20*, 2887-2900, 2006.
- 733 Fichter, J., Turpault, M. P., Dambrine, E. and Ranger, J.: Mineral evolution of acid forest soils in the
734 Strengbach catchment (Vosges mountains, NE France), *Geoderma*, *82*, 315-340, 1998.
- 735 Fischer, C., Kurganskaya, I., Schäfer, T. and Lüttge, A.: Variability of crystal surface reactivity: What do we
736 know?, *Applied Geochem.* *43*, 132-157, 2014.



- 737 Fritz, B., Clément, A., Amal, Y. and Noguera, C.: Simulation of the nucleation and growth of simple clay
738 minerals in weathering processes : the NANOKIN Code, *Geochim. Cosmochim. Acta*, 73, 1340-
739 1358, 2009.
- 740 Gangloff, S., Stille, P., Schmitt, A.D. and Chabaux F.: Factors controlling the chemical composition of
741 colloidal and dissolved fractions in soil solutions and the mobility of trace elements in soils,
742 *Geochim. Cosmochim. Acta*, 189 37–57, 2016.
- 743 Gangloff, S., Stille, P., Pierret, M. C., Weber, T. and Chabaux, F. : Characterization and evolution of
744 dissolved organic matter in acidic forest soil and its impact on the mobility of major and trace
745 elements (case of the Strengbach watershed), *Geochim. Cosmochim. Acta*, 130, 21-41, 2014.
- 746 Gautier, J. M., Oelkers, E. H. and Schott, J.: Are quartz dissolution rates proportional to BET surface
747 areas?, *Geochim. Cosmochim. Acta*, 65, 1059-1070, 2001.
- 748 Gérard, F., Clément, A. and Fritz, B.: Numerical validation of a Eulerian hydrochemical code using a 1D
749 multisolute mass transport system involving heterogeneous kinetically controlled reactions, *J.*
750 *Cont. Hydrol.*, 30, 201-216, 1998.
- 751 Gh'Mari, E. : *Etude minéralogique, pétrophysique et géochimique de dynamique d'altération d'un granite*
752 *soumis aux dépôts atmosphériques acides (bassin versant du Strengbach, Vosges, France).*
753 *Mécanismes, bilans et modélisation*, PhD Thesis,, Université Louis Pasteur, Strasbourg, pp. 200.
- 754 Gislason, S. R., Oelkers, E. H., Eiriksdottir, E. S., Kardjilov, M. I., Gisladottir, G., Sigfusson, B., Snorrason, A.,
755 Elefsen, S., Hardardottir, J., Torssander, P. and Oskarsson, N.: Direct evidence of the feedback
756 between climate and weathering, *Earth Planet. Sci. Lett.*, 277, 213-222, 2009.
- 757 Goddérés, Y., François, L. M., Probst, A., Schott, J., Moncoulon, D., Labat, D. and Viville, D.: Modelling
758 weathering processes at the catchment scale: the WITCH numerical model, *Geochim.*
759 *Cosmochim. Acta* 70, 1128–1147, 2006.



- 760 Godd ris, Y., Brantley, S. L., Fran ois, L., Schott, J., Pollard, D., D qu , M. and Dury, M.: Rates of
761 consumption of atmospheric CO₂ through the weathering of loess during the next 100 yr of
762 climate change, *Biogeosciences*, *10*, 135-148, 2013.
- 763 Godsey, S. E., Kirchner, J. W., and Clow, D. W.: Concentration–discharge relationships reflect chemostatic
764 characteristics of US catchments. *Hydrological Processes: An International Journal*, *23*, 1844-
765 1864, 2009.
- 766 Guidry, M. W. and Mackenzie, F. T.: Experimental study of igneous and sedimentary apatite dissolution:
767 control of pH, distance from equilibrium, and temperature on dissolution rates, *Geochim.*
768 *Cosmochim. Acta*, *67*, 2949-2963, 2003.
- 769 Gunduz, O. and Aral, M. M.: River networks and groundwater flow: a simultaneous solution of a coupled
770 system, *J. Hydrol.*, *301*, 216-234, 2005.
- 771 Hazenberg, P., Broxton, P., Gochis, D., Niu, G. Y., Pangle, L. A., Pelletier, J. D., ... and Zeng, X. (2016).
772 Testing the hybrid-3-D hillslope hydrological model in a controlled environment, *Wat. Resour.*
773 *Res.*, *52*, 1089-1107, 2016.
- 774 Jeannot, B., Weill, S., Eschbach, D., Schmitt, L. and Delay, F.: A low-dimensional integrated subsurface
775 hydrological model coupled with 2-D overland flow: Application to a restored fluvial
776 hydrosystem (Upper Rhine River–France), *J. Hydrol.*, *563*, 495-509, 2018.
- 777 Kampf, S. K. and Burges, S. J.: A framework for classifying and comparing distributed hillslope and
778 catchment hydrologic models, *Water Resour. Res.*, W05423, doi:10.1029/2006WR005370, 2007
- 779 Kim, H., Dietrich, W. E., Thurnhoffer, B. M., Bishop, J. K. and Fung, I. Y.: Controls on solute concentration-
780 discharge relationships revealed by simultaneous hydrochemistry observations of hillslope
781 runoff and stream flow: The importance of critical zone structure, *Water Resour. Res.*, *53*, 1424-
782 1443, 2017.



- 783 Kirchner, J. W.: Getting the right answers for the right reasons: Linking measurements, analyses, and
784 models to advance the science of hydrology, *Water Resour. Res.* **42**, W03S04,
785 doi:10.1029/2005WR004362, 2006.
- 786 Larsen, I. J., Almond, P. C., Eger, A., Stone, J. O., Montgomery, D. R. and Malcolm, B.: Rapid soil
787 production and weathering in the Western Alps, New Zealand, *Science*, 1244908, 2014.
- 788 Lebedeva, M. I. and Brantley, S. L. : Exploring geochemical controls on weathering and erosion of convex
789 hillslopes: Beyond the empirical regolith production function. *Earth Surface Processes and*
790 *Landforms*, **38**, 1793-1807, 2013.
- 791 Li, D. D., Jacobson, A. D. and McInerney, D. J.: A reactive-transport model for examining tectonic and
792 climatic controls on chemical weathering and atmospheric CO₂ consumption in granitic regolith.
793 *Chem. Geol.*, **365**, 30-42 2014.
- 794 Li, L., Peters, C. A. and Celia, M. A.: Upscaling geochemical reaction rates using pore-scale network
795 modeling. *Advances in water resources*, **29**, 1351-1370, 2006.
- 796 Li, L., Maher, K., Navarre-Sitchler, A., Druhan, J., Meile, C., Lawrence, C., ... and Jin, L. : Expanding the role
797 of reactive transport models in critical zone processes. *Earth-Science Reviews*, **165**, 280-301,
798 2017
- 799 Lucas, Y., Schmitt, A. D., Chabaux, F., Clément, A., Fritz, B., Elsass, P. and Durand, S.: Geochemical tracing
800 and hydrogeochemical modelling of water–rock interactions during salinization of alluvial
801 groundwater (Upper Rhine Valley, France), *Appl. Geochem.*, **25**, 1644-1663, 2010.
- 802 Lucas, Y., Chabaux, F., Schaffhauser, T., Fritz, B., Ambroise, B., Ackerer, J. and Clément, A.:
803 Hydrogeochemical modeling (KIRMAT) of spring and deep borehole water compositions in the
804 small granitic Ringelbach catchment (Vosges Mountains, France), *Applied Geochemistry*, **87**, 1-
805 21, 2017.



- 806 Lundström, U. and Öhman, L. O.: Dissolution of feldspars in the presence of natural, organic solutes,
807 *Journal of Soil Science*, *41*, 359-369, 1990.
- 808 Maher, K., Steefel, C. I., White, A. F., & Stonestrom, D. A.: The role of reaction affinity and secondary
809 minerals in regulating chemical weathering rates at the Santa Cruz Soil Chronosequence,
810 California, *Geochim. Cosmochim. Acta*, *73*, 2804-2831, 2009.
- 811 Maher, K. : The dependence of chemical weathering rates on fluid residence time, *Earth Planet. Sci. Lett.*,
812 *294*, 101-110, 2010.
- 813 Maher, K.: The role of fluid residence time and topographic scales in determining chemical fluxes from
814 landscapes, *Earth Planet. Sci. Let.*, *312*, 48-58, 2011.
- 815 Mirus, B. B., Ebel, B. A., Heppner, C. S. and Loague, K.: Assessing the detail needed to capture rainfall-
816 runoff dynamics with physics-based hydrologic response simulation, *Water Resour. Res.*, *47*,
817 W00H10, doi:10.1029/2010WR009906, 2011
- 818 Moore, J., Lichtner, P. C., White, A. F. and Brantley, S. L.: Using a reactive transport model to elucidate
819 differences between laboratory and field dissolution rates in regolith, *Geochim. Cosmochim.*
820 *Acta*, *93*, 235-261, 2012.
- 821 Navarre-Sitchler, A. and Brantley, S.: Basalt weathering across scales, *Earth and Planet. Sci. Let.*, *261*,
822 321-334, 2007.
- 823 Navarre-Sitchler, A., Steefel, C. I., Yang, L., Tomutsa, L. and Brantley, S. L.: Evolution of porosity and
824 diffusivity associated with chemical weathering of a basalt clast, *Journal of Geophysical Research:*
825 *Earth Surface*, *114*, F02016, doi:10.1029/2008JF001060, 2009.
- 826 Ngo, V. V., Delalande, M., Clément, A., Michau, N. and Fritz, B.: Coupled transport-reaction modeling of
827 the long-term interaction between iron, bentonite and Callovo-Oxfordian claystone in
828 radioactive waste confinement systems., *Applied Clay Science*, *101*, 430-443, 2014



- 829 Noguera, C., Fritz, B. and Clément, A.: Simulation of the nucleation and growth of clay minerals coupled
830 with cation exchange, *Geochim. Cosmochim. Acta*, 75, 3402-3418, 2011.
- 831 Pan, Y., Weill, S., Ackerer, P. and Delay, F.: A coupled stream flow and depth-integrated subsurface flow
832 model for catchment hydrology, *Journal of Hydrology*, 530, 66-78, 2015
- 833 Pierret, M. C., Stille, P., Prunier, J., Viville, D. and Chabaux, F. : Chemical and U–Sr isotopic variations in
834 stream and source waters of the Strengbach watershed (Vosges mountains, France). *Hydrology
835 and Earth System Sciences*, 18, 3969-3985, 2014.
- 836 Pollet-Villard, M., Daval, D., Ackerer, P., Saldi, G. D., Wild, B., Knauss, K. G. and Fritz, B.: Does
837 crystallographic anisotropy prevent the conventional treatment of aqueous mineral reactivity? A
838 case study based on K-feldspar dissolution kinetics, *Geochim. Cosmochim. Acta*, 190, 294-308,
839 2016.
- 840 Prunier, J., Chabaux, F., Stille, P., Gangloff, S., Pierret, M. C., Viville, D. and Aubert, A. : Geochemical and
841 isotopic (Sr, U) monitoring of soil solutions from the Strengbach catchment (Vosges mountains,
842 France): Evidence for recent weathering evolution, *Chem. Geol.*, 417, 289-305, 2015.
- 843 Schaffhauser, T., Chabaux, F., Ambroise, B., Lucas, Y., Stille, P., Reuschlé, T., Perrone, T. and Fritz, B.:
844 Geochemical and isotopic (U, Sr) tracing of water pathways in the granitic Ringelbach catchment
845 (Vosges Mountains, France), *Chem. Geol.*, 374, 117-127, 2014.
- 846 Schmitt, A.D., Gangloff, S., Labolle, F., Chabaux, F. and Stille, P.: Ca biogeochemical cycle at the beech
847 tree - soil solution interface from the Strengbach CZO (NE France): insights from stable Ca and
848 radiogenic Sr isotopes, *Geochim. and Cosmochim. Acta* 213, 91-109, 2017
- 849 Schmitt AD, Borrelli N., Ertlen D., Gangloff S., Chabaux, F. and Osterrieth M.: Stable calcium isotope
850 speciation and calcium oxalate production within beech tree (*Fagus sylvatica* L.) organs,
851 *Biogeochemistry*, 137,197-217, DOI 10.1007/s10533-017-0411-0, 2018.



- 852 Steefel, C. I., DePaolo, D. J. and Lichtner, P. C.: Reactive transport modeling: An essential tool and a new
853 research approach for the Earth sciences, *Earth Planet. Sci. Let.*, *240*, 539-558, 2005
- 854 Tardy, Y. and Fritz, B.: An ideal solid solution model for calculating solubility of clay minerals, *Clay*
855 *minerals*, *16*, 361-373, 1981.
- 856 Viville, D., Chabaux, F., Stille, P., Pierret, M. C. and Gangloff, S.: Erosion and weathering fluxes in granitic
857 basins: the example of the Strengbach catchment (Vosges massif, eastern France), *Catena*, *92*,
858 122-129, 2012.
- 859 Weill, S., Altissimo, M., Cassiani, G., Deiana, R., Marani, M. and Putti, M.: Saturated area dynamics and
860 streamflow generation from coupled surface–subsurface simulations and field observations,
861 *Advances in water resources*, *59*, 196-208, 2013.
- 862 Weill, S., Delay, F., Pan, Y. and Ackerer, P.: A low-dimensional subsurface model for saturated and
863 unsaturated flow processes: ability to address heterogeneity, *Computational Geosciences*, *21*,
864 301-314, 2017.
- 865 White, A. F. and Brantley, S. L.: The effect of time on the weathering of silicate minerals: why do
866 weathering rates differ in the laboratory and field?, *Chem. Geol.*, *202*, 479-506, 2003.
- 867 Wild, B., Daval, D., Guyot, F., Knauss, K. G., Pollet-Villard, M. and Imfeld, G.: pH-dependent control of
868 feldspar dissolution rate by altered surface layers, *Chemical Geology*, *442*, 148-159, 2016
- 869 Zhu, C.: In situ feldspar dissolution rates in an aquifer, *Geochim. Cosmochim. Acta*, *69*, 1435-1453, 2005
- 870
- 871



872 **Figure captions**

873 Figure 1: sampling locations within the Strengbach catchment. Blue stars represent springs, blue
874 diamonds represent piezometers, and the blue circle represents the stream at the outlet of the
875 watershed. Green circles represent soil solution locations, and black diamonds represent
876 bedrock facies locations.

877 Figure 2: on the left: field of thicknesses of the weathered material constituting the shallow
878 unconfined aquifer at the Strengbach catchment used for the simulations of NIHM. The 1D
879 surface draining network used in NIHM is represented by the black lines. On the right: fitting
880 observed flow rates from the Strengbach stream at the outlet of the catchment with simulations
881 of flow within the watershed (illustrated from 2010 to 2015). The subsurface compartment
882 inherits from the aquifer thicknesses reported in the left panel, and the topography makes the
883 natural outlet of the subsurface compartment the surface draining network.

884 Figure 3: principle of the method of backtracking used to determine flow lines that generate
885 flow at the outlet of the Strengbach catchment. Particles are dispatched along the dry fraction
886 of the 1D river network (only one is represented here at a position a on 01/01/2010 at 23:59).
887 NIHM generates an output heterogeneous velocity field at that date for the whole watershed,
888 denoted $V_{01/01/2010}$. By applying a velocity field of the same magnitude but opposite direction to
889 the particle, the position of the particle can be backtracked until 31/12/2009 23:59. Then, to
890 further backtrack the trajectory of the particle, the velocity field is updated accordingly. The
891 frequency of updating of the velocity field was set to 1 day, as a compromise between the
892 accuracy of results and computational time considerations.



893 Figure 4: at the top, flow lines of the subsurface that feed with water the surface draining
894 network on March 1st, 2010 (on the left, high-flow period) and July 1st, 2010 (on the right, low-
895 flow period). The color scale indicates that a water particle reaching the river at a given date
896 started its travel along the streamline or passed at a given location on the streamline x days
897 before. The density of streamlines is associated with the flowing versus dry fraction of the river
898 network at a prescribed date. Below, flow lines of the subsurface that feed with water the
899 geochemical sampling sites on March 30th, 2010 (on the left, flood event) and November 29th,
900 2011 (right, drought event) according to NIHM simulations. For each sampling site, 10 particles
901 were dispatched in the direct neighborhood of the site and then backtracked. The color scale
902 indicates that a water particle reaching the sampling site at a given date started its travel along
903 the streamline or passed at a given location on the streamline x days before.

904 Figure 5: conceptual scheme used in the modeling of the water chemistry. The soil solutions are
905 used as input solution. The bedrock is discretized into a 1D succession of cells along the active
906 parts of the flow lines previously determined by the hydrological NIHM model. Within each cell,
907 the geochemical and transport equations are numerically solved using the KIRMAT
908 hydrogeochemical code. To calculate the integrated chemical composition of the spring water,
909 several simulations with different entering points of soil solutions along the flow path were
910 performed, and the integrated chemistry was calculated by taking the arithmetic mean of all the
911 simulated solute concentrations.

912 Figure 6: maps of piezometric gradient and mean hydraulic conductivity for the Strengbach
913 catchment, as simulated by NIHM, on 29/11/2011 (dry period) and 30/03/2010 (high flows



914 period). The mean hydraulic conductivity is the mean of all hydraulic conductivities integrated
915 over the depth of the aquifer and thus depends on the water saturation.

916 Figure 7: simulation results for the CS1 spring for an important drought (29/11/2011) and a
917 strong flood event (30/03/2010). At the top, active parts of the flow lines that bring the waters
918 to the CS1 spring for the two sampling dates. Below, simulated chemical compositions of the
919 CS1 spring waters after integration along the flow lines and a comparison with the initial soil
920 solution and the spring chemistry data are presented.

921 Figure 8: simulation results for the CS1 spring over the whole range of the water discharges
922 from the spring. Red lines indicate simulated parameters after integration along the flow lines,
923 and blue points show measured values from the field campaigns realized between 2005 and
924 2015.

925 Figure 9: simulation results for the PZ3 and PZ5 piezometers for a strong flood event
926 (05/05/2015). At the top, active parts of the flow lines that bring the waters to the two sampling
927 sites are shown. Below, simulated chemical compositions of the piezometer waters after
928 integration along the flow lines and a comparison with the initial soil solution and the water
929 chemistry data are presented.

930 Figure 10: simulation results for the CS2 spring. At the top, active parts of the flow lines that
931 bring the waters to the CS2 spring for an important drought (29/11/2011) and a strong flood
932 event (30/03/2010) are shown. The location of the CS2 spring implies a more scattered
933 distribution of the flow lines than for the CS1 spring. Below, simulation results for the CS2 spring
934 over the whole range of the water discharges from the spring are presented. Blue lines indicate



935 simulated parameters after integration along the slowest flow line, yellow lines indicate
936 simulated parameters after integration along the fastest flow line, and blue points show
937 measured values from the field campaigns realized between 2005 and 2015.

938 Figure 11: simulation results for the RH3 spring chemistry and for a flood event (30/03/2010).
939 On the left, simulated concentrations for the case assuming that the flow lines only run on
940 gneiss (GN) are shown. On the right, simulated concentrations for the case assuming that the
941 flow lines only run on hydrothermally altered granite (VS) are presented.

942 Figure 12: overview of the flow lines of the subsurface that feed with water the geochemical
943 sampling sites CS1, PZ3 and PZ5 on May 5th, 2015 according to the NIHM simulations. The
944 simulated chemical compositions after geochemical integration along the flow lines are also
945 presented for this transect on the southern part of the watershed (CS1, PZ3 and PZ5) and
946 compared with the initial soil solution and the spring chemistry data.

947 Table 1: measured pH, water discharges and chemical concentrations of H_4SiO_4 , Na^+ , K^+ , Mg^{2+} ,
948 and Ca^{2+} in the waters collected from the sampling sites in the Strengbach catchment. The
949 sampling sites include springs (CS1, CS2, RH3) and piezometers (PZ3, PZ5).

950 Table 2: Comparison between BET surfaces and geometric surfaces for the major primary
951 minerals present in a granitic context. BET surfaces were measured via gas absorption
952 experiments by ¹Berger et al., 1994; ²Chou and Wollast, 1985; ³Lundstrom and Ohman, 1990; ⁴
953 Amrhein and Suarez, 1992; ⁵Acker and Bricker, 1992; and ⁶Guidry and Mackenzie, 2003.
954 Geometric surfaces were recalculated from the granulometric ranges of the minerals and by
955 assuming a spherical geometry.



	Na ⁺ (mmol/L)	K ⁺ (mmol/L)	Mg ²⁺ (mmol/L)	Ca ²⁺ (mmol/L)	H ₄ SiO ₄ (mmol/L)	pH	Water Discharge (L/s)
Spring CS1							
16/09/2008	0.071	0.013	0.017	0.044	0.129	6.28	0.954
30/03/2010	0.074	0.014	0.015	0.043	0.120	5.61	1.523
29/03/2011	0.074	0.013	0.015	0.038	0.145	6.23	0.345
04/10/2011	0.080	0.012	0.016	0.042	0.176	6.57	0.122
29/11/2011	0.088	0.015	0.019	0.034	0.177	6.30	0.098
05/05/2015	0.065	0.012	0.012	0.054	0.121	5.33	1.410
Spring CS2							
30/03/2010	0.090	0.020	0.020	0.080	0.122	6.15	6.274
29/03/2011	0.090	0.020	0.020	0.070	0.144	6.18	0.956
02/08/2011	0.090	0.020	0.020	0.060	0.170	6.50	2.171
04/10/2011	0.100	0.020	0.020	0.070	0.177	6.76	0.413
29/11/2011	0.100	0.020	0.020	0.060	0.180	6.22	0.285
05/05/2015	0.077	0.016	0.018	0.074	0.123	6.14	7.500
Spring RH3							
30/03/2010	0.083	0.028	0.032	0.081	0.127	6.28	-
Piezometer PZ3							
05/05/2015	0.074	0.013	0.011	0.053	0.153	6.29	-
Piezometer PZ5							
05/05/2015	0.072	0.013	0.017	0.058	0.132	6.16	-

Table 1



Mineral	Mineral density (g/cm ³)	Granulometric range (μm)	Particle radius (μm)	Spherical geometric surface (m ² /g)	BET surface (m ² /g)
Quartz ¹	2.62	< 50	1 - 25	1.150 - 0.046	0.310
Albite ²	2.60	50 - 100	25 - 50	0.046 - 0.023	0.075
K-feldspar ³	2.56	< 50	1 - 25	1.170 - 0.047	1.420
Anorthite ⁴	2.73	20 - 50	10 - 25	0.044 - 0.111	0.500
Biotite ⁵	3.09	150 - 400	75 - 200	0.013 - 0.005	0.240
Apatite ⁵	3.19	100 - 200	50 - 100	0.018 - 0.009	0.026

Table 2

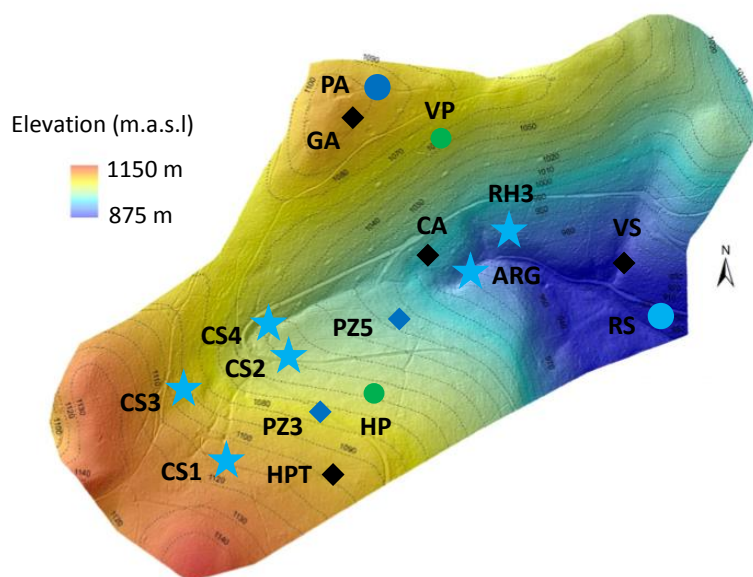


Figure 1

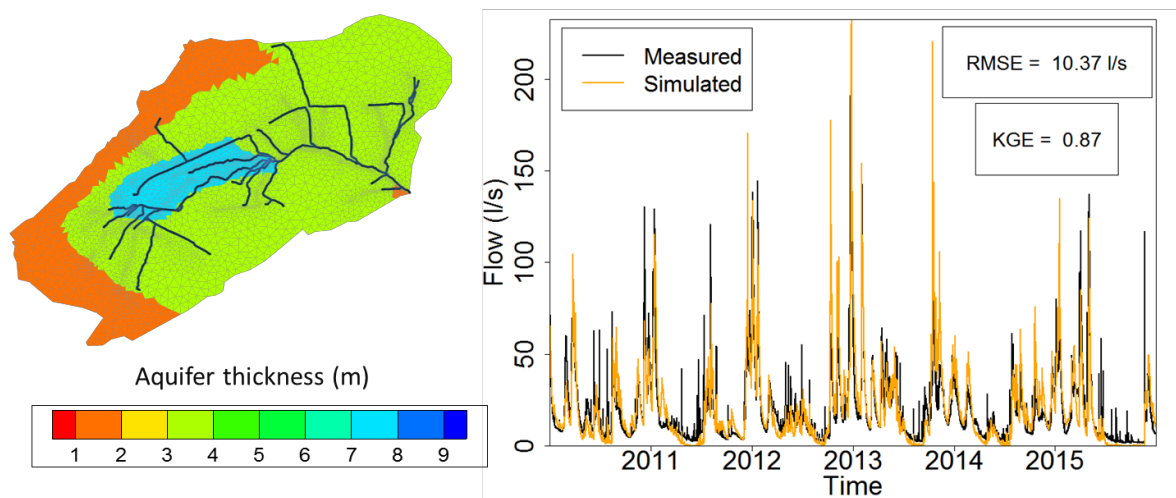


Figure 2

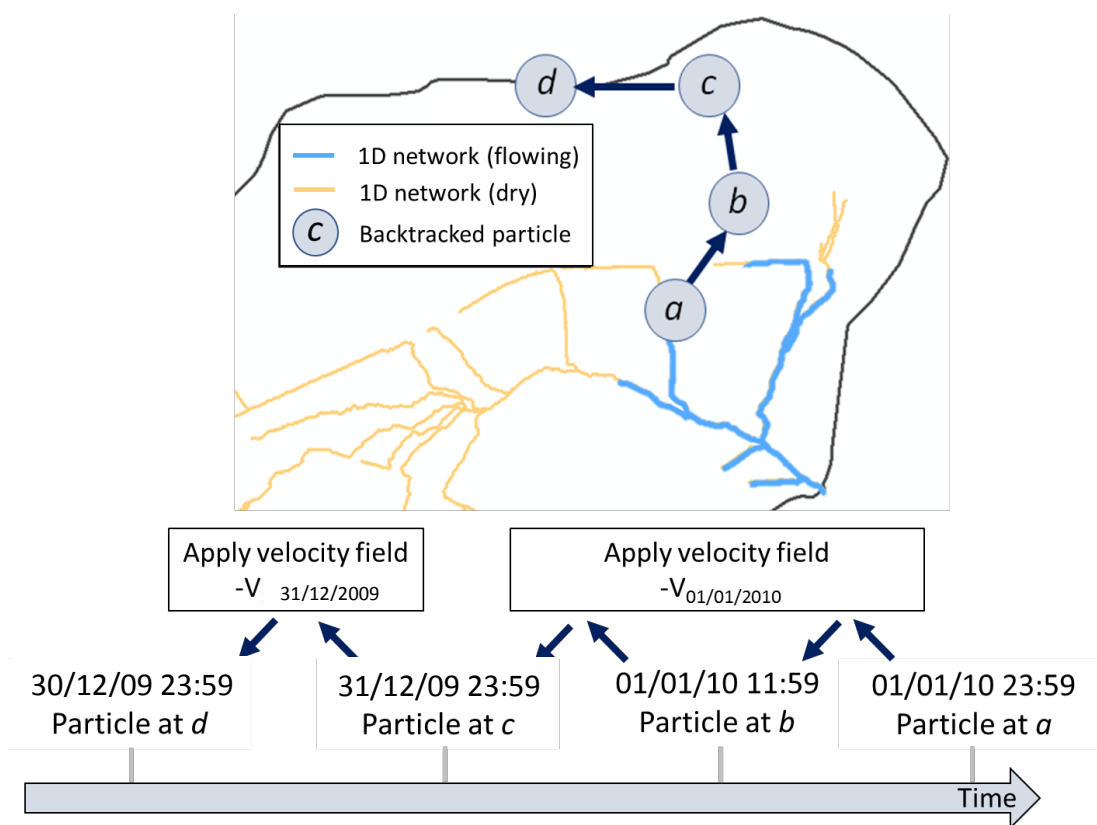


Figure 3

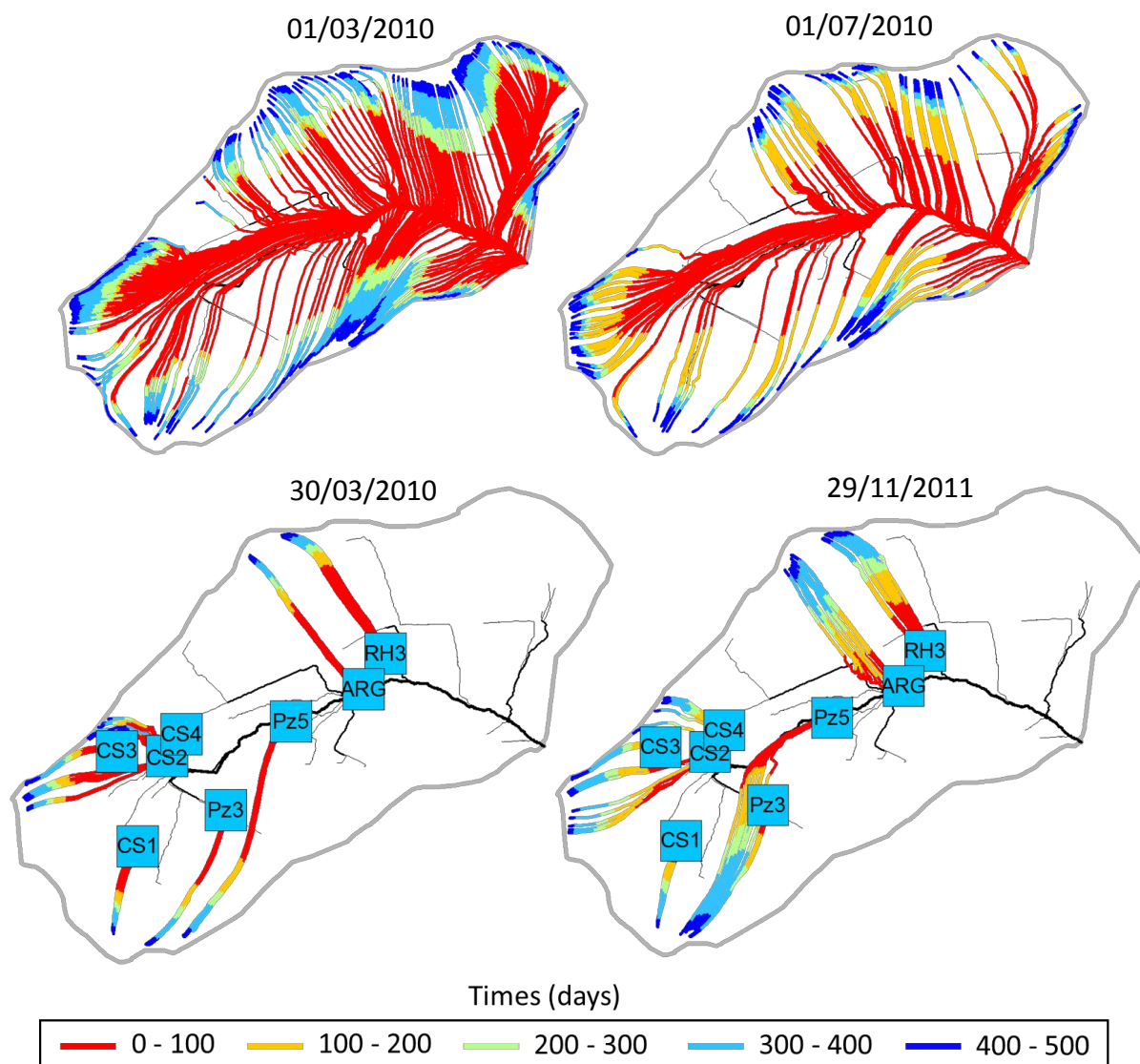


Figure 4

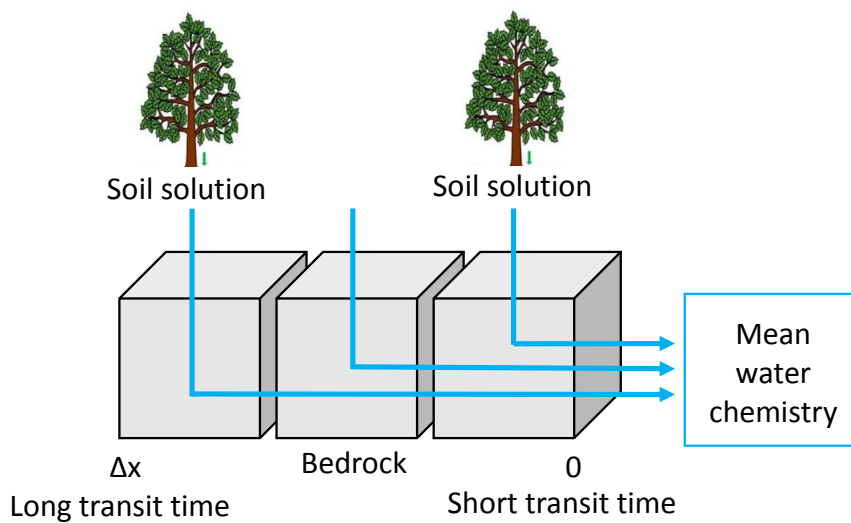


Figure 5

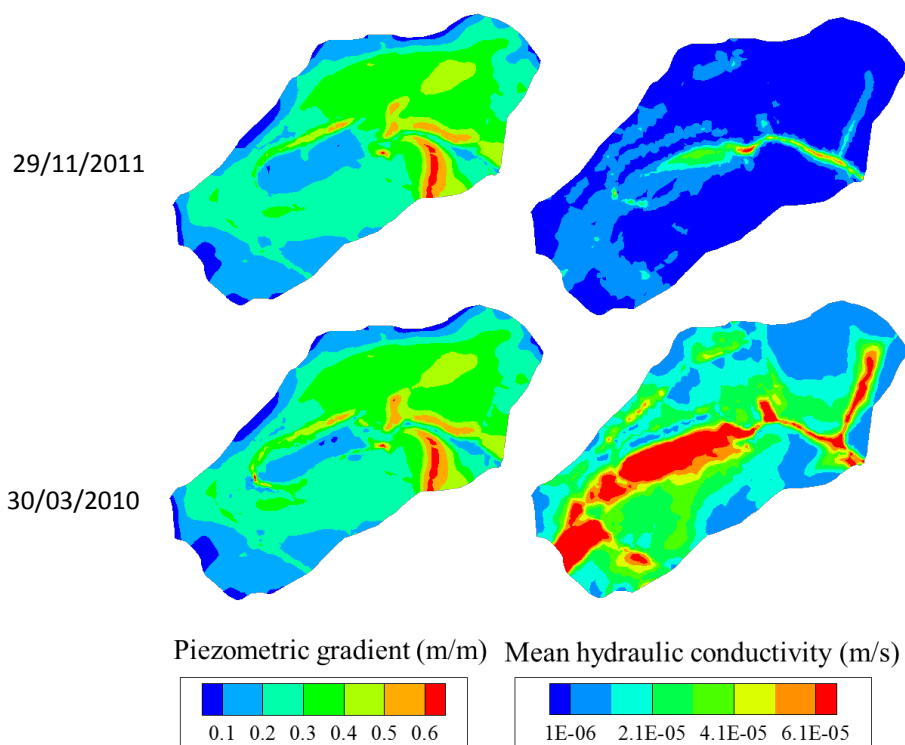


Figure 6

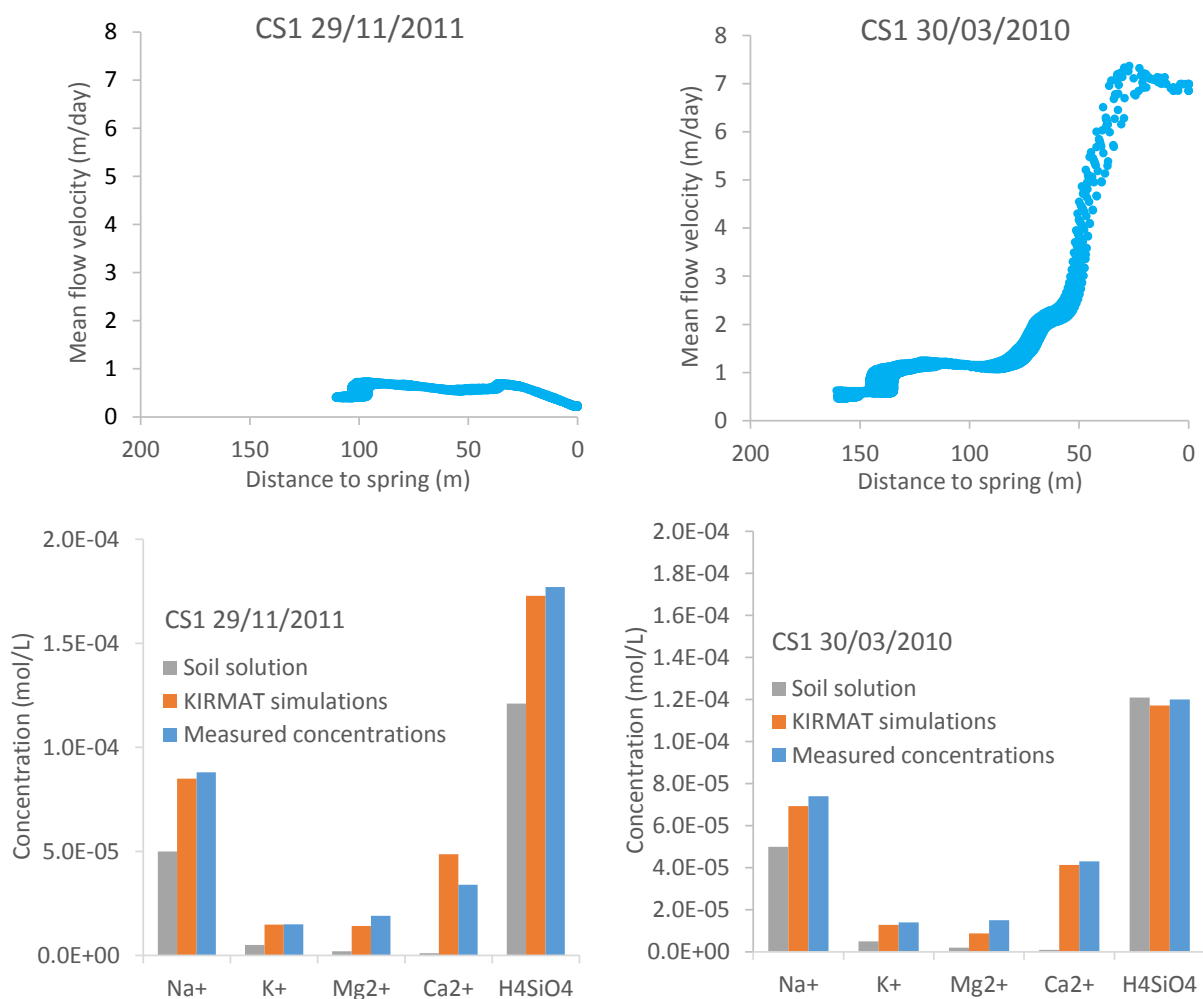


Figure 7

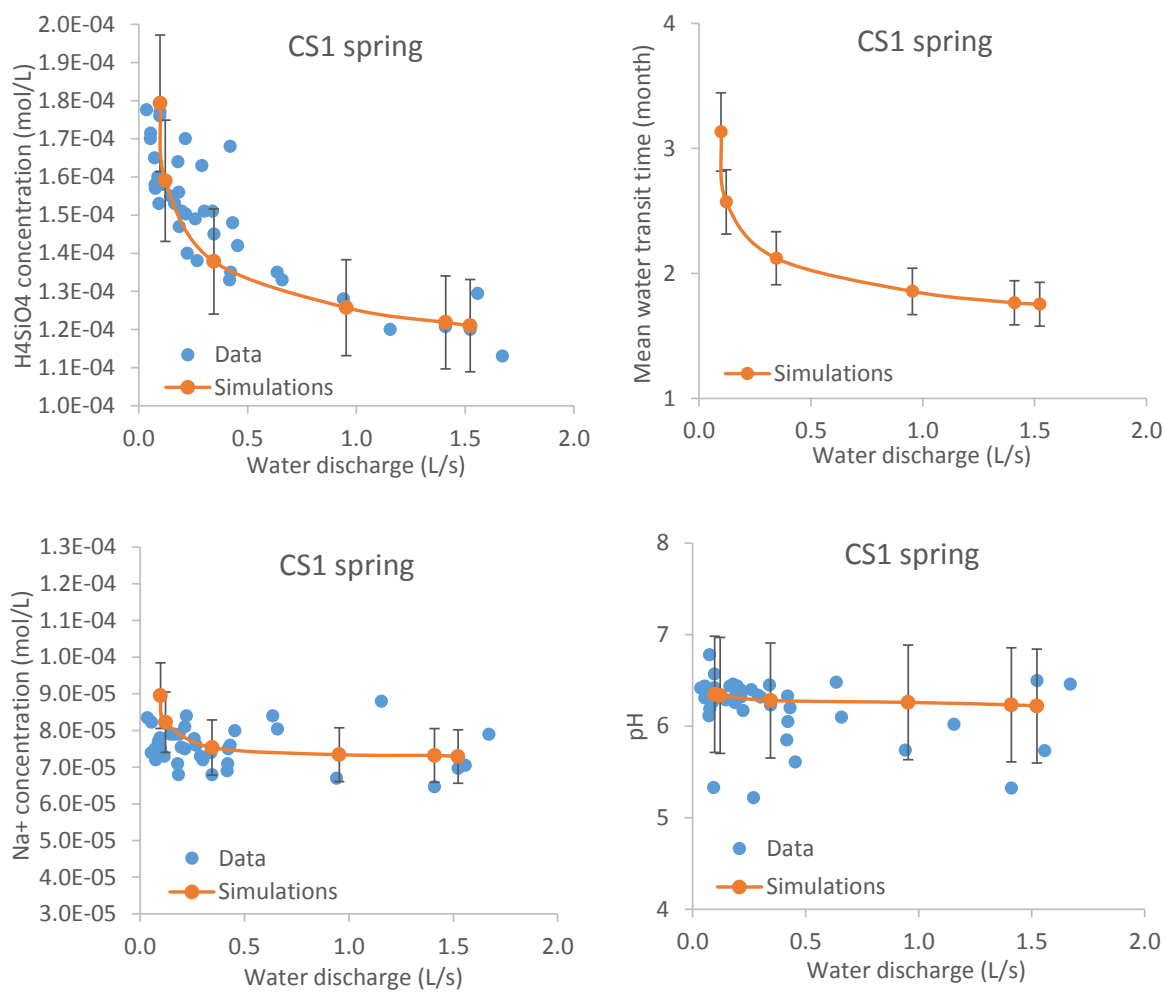


Figure 8

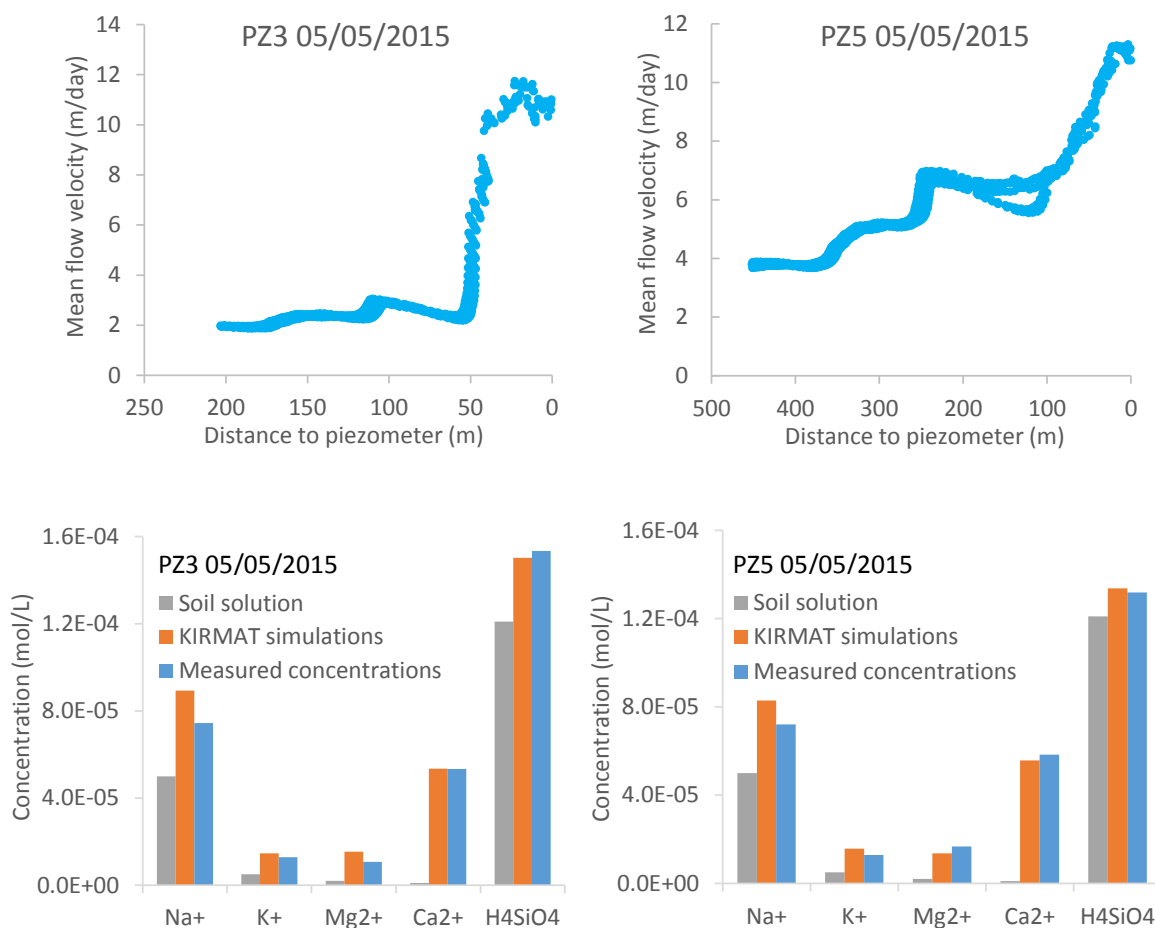


Figure 9

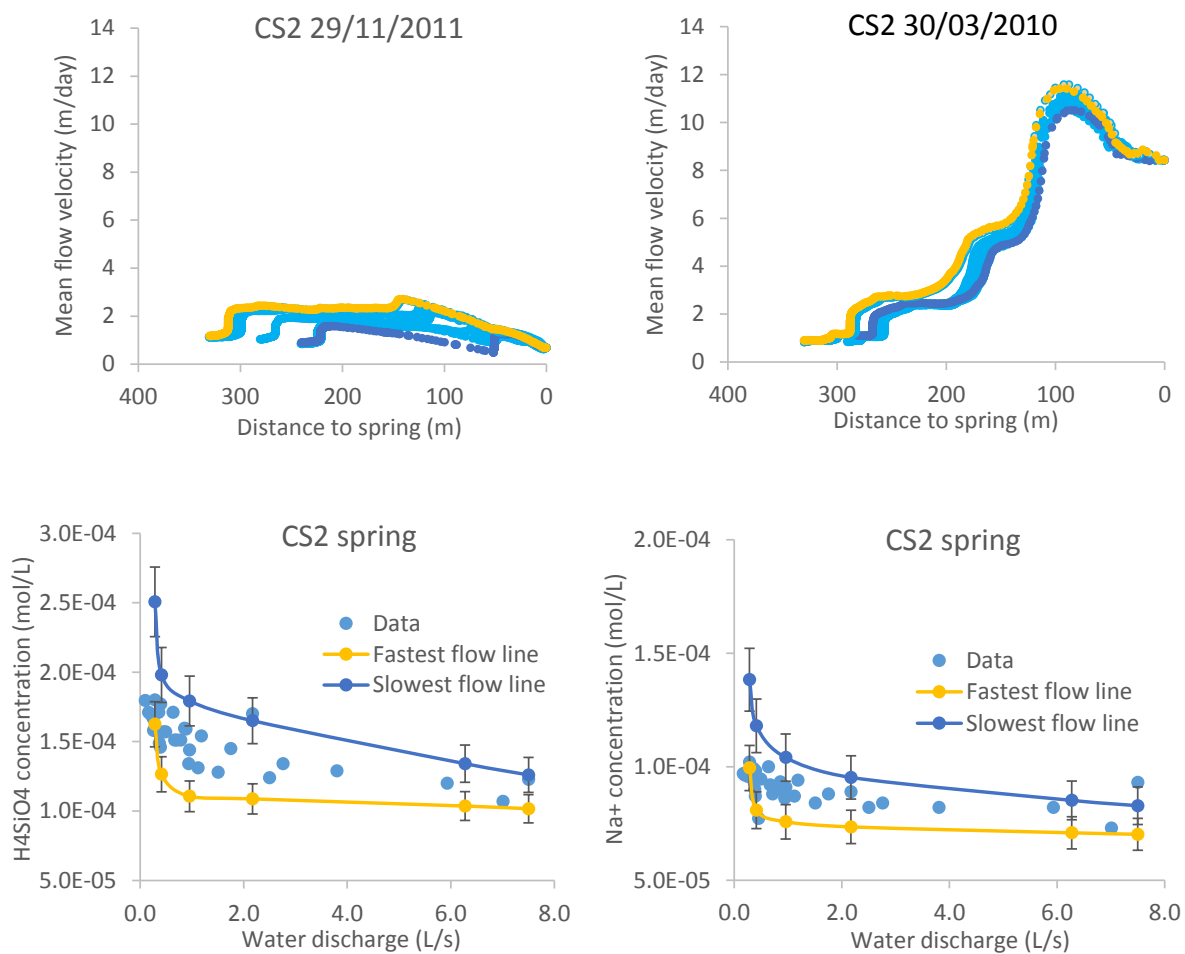


Figure 10

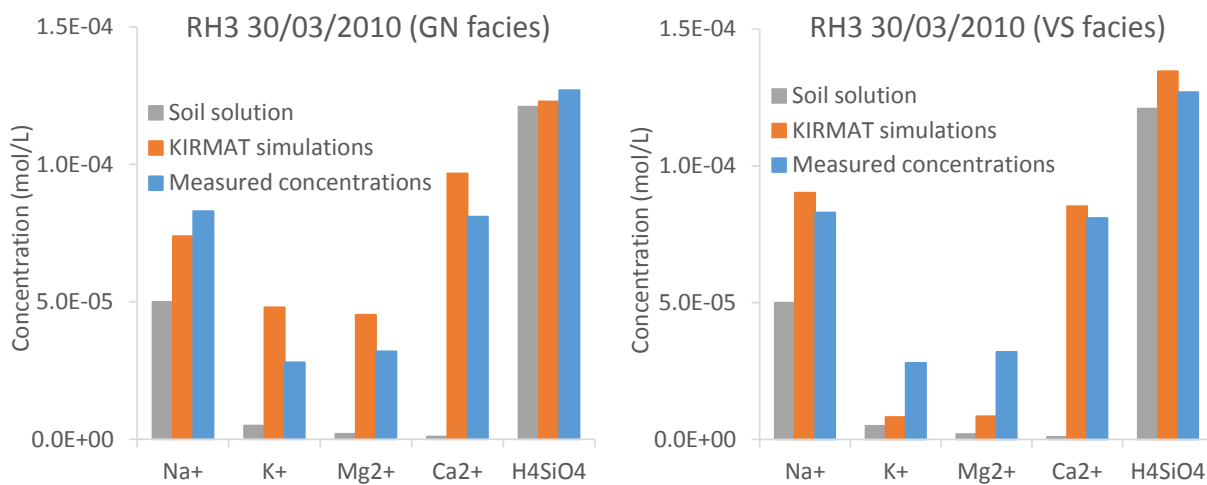


Figure 11

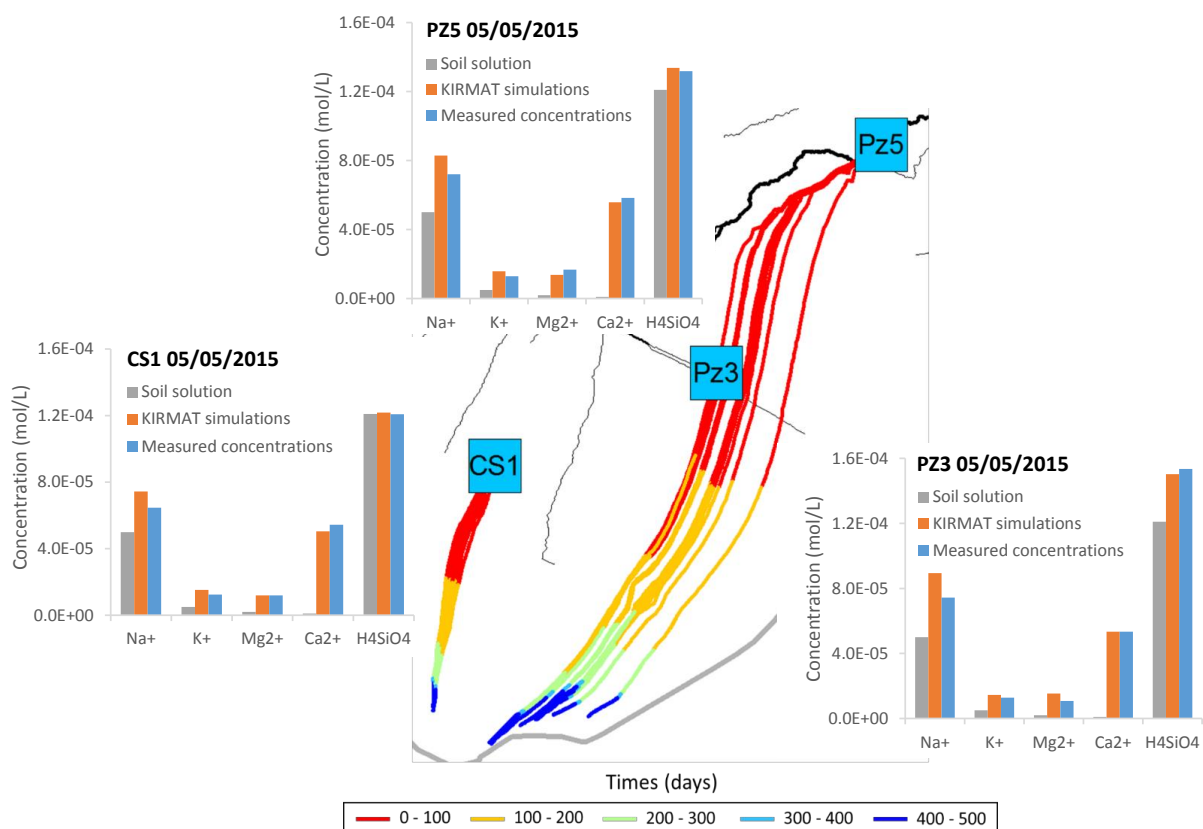


Figure 12